JOURNAL OF GEOPHYSICAL RESEARCH, VOL. 113, B12412, doi:10.1029/2008JB005717, 2008

Click Here for Full Article

# Prediction of thrusting sequences in accretionary wedges

N. Cubas,[1] Y. M. Leroy,[1] and B. Maillot[2]

Received 25 March 2008; revised 1 September 2008; accepted 7 October 2008; published 27 December 2008.

[1] The main objective is to determine the three stages of the life of a thrust in an accretionary wedge which are the onset of thrusting along its ramp, the development with the construction of the relief, and the arrest because of the onset of another thrusting event. A simple kinematics is proposed for the geometry of the developing thrust fold based on rigid regions separated by velocity discontinuities along which work is dissipated according to the Coulomb criterion. The evolution of the thrust fold satisfies mechanical equilibrium and is optimized at every time of the three stages to provide the least upper bound in tectonic force according to the maximum strength theorem. The development of the thrust or its arrest because of the initiation of another thrust is decided by selecting the event which leads to the least upper bound in tectonic force. The approach is first validated by proving that the critical slope angle $\alpha_c$ for the classical triangular wedge is properly captured. It is shown that a perturbation, in the form of an extra relief in this perfectly triangular geometry, leads to the onset of thrusting with the ramp or the back thrust outcropping either at the back or to the front of the perturbation, respectively, for a range of slope dip close to the critical angle $\alpha_c$. The study of normal thrust sequences (from the rear to the front in the wedge toe) reveals that weakening of the ramp, accounted for by changing its friction angle from an initial to a smaller final value, is necessary for each thrust to have a finite life span. This life span is longer with a larger relief buildup for more pronounced weakening. Decreasing the décollement friction angle results in an increase in the number of thrusts in the sequence, each thrust creating milder relief. The normal sequence is ended with the first out of sequence thrust which occurs earlier for smaller weakening over the ramp. The proposed methodology is partly used to construct an inverse method proposed to assess the likeliness for the transfer of activity from the active to the incipient thrust in a section of Nankai's accretionary wedge. The inverse method provides the initial friction angle over the incipient ramp and the final friction angle over the fully active ramp, from the geometry of the corresponding thrusts, and the topography. It is shown that the friction angle over the incipient ramp is most likely to be larger then the one over the active ramp, justifying a key hypothesis needed to predict discrete sequences of thrusting.

**Citation:** Cubas, N., Y. M. Leroy, and B. Maillot (2008), Prediction of thrusting sequences in accretionary wedges, *J. Geophys. Res.*, *113*, B12412, doi:10.1029/2008JB005717.

## 1. Introduction

[2] The objective of this research is to propose simple quantitative methods to study the development of multiple thrusts in accretionary wedges and fold-and-thrust belts. The method should require less computational times than the finite element method so that repeated (thousands) tests can be performed, typically in inverse analyses. It should also provide quantitative predictions of the position and dip of the active thrusts, a task which cannot be performed with classical geometrical models of folding.

[3] Predicting fault patterns in accretionary wedges has its roots in the stability of a perfect triangular wedge. Faulting occurs according to the active and passive Rankine stress states, as shown analytically by *Davis et al.* [1983], *Dahlen* [1984], and with a Mohr construction by *Lehner* [1986]. The main result is that there is a critical taper value above which the entire décollement is activated upon compression from the back stop. The wedge is said to be unstable for angles below that critical value and the deformation is then to the rear. This reasoning applies to the onset of failure in a perfectly triangular prism and is not valid for any irregular topography. Note that at the critical taper, the fault positions are undetermined if the failure criterion is cohesionless [*Dahlen*, 1984]. Introducing bulk cohesion

[1]Laboratoire de Géologie, CNRS, Ecole Normale Supérieure, Paris, France.
[2]Laboratoire de Tectonique, CNRS, Université de Cergy-Pontoise, Cergy-Pontoise, France.

Copyright 2008 by the American Geophysical Union.
0148-0227/08/2008JB005717$09.00

sets in a characteristic length scale, leading *Yin* [1993] to predict the position of the first thrust in the triangular wedge, using the stress approach proposed by *Hafner* [1951] for linear elastic materials. The elasticity solution for irregular topography is still possible if the variations in slope are small, permitting the application of linear perturbation techniques [*McTigue and Mei*, 1981]. This approach combined with a numerical solution by Fast Fourier Transform leads *Panian and Pilant* [1990] to predict that first failure is below the topographic front of the wedge.

[4] These solutions cannot however be applied for thrusting beyond the onset. The first prediction of a complete thrusting sequence seems to be due to *Platt* [1988, 1990] based on simple geometrical rules, reminiscent of Suppe's construction [*Suppe*, 1983] and on an insight on the stress distribution. He also predicts that the position of the new thrust is controlled by the topography. The active thrust within the sequence is then chosen to keep the entire wedge close to the critical taper. Another approach is proposed by *Outtani* [1996], *Hardy et al.* [1998], and *Masek and Duncan* [1998], who control the thrusting evolution by comparing the various potential scenarios in terms of dissipation. The thrusting leading to the least dissipation by friction over predefined discontinuity segments [*Masek and Duncan*, 1998] is favored at any step of the shortening. Similar ideas are found in the work of *Gutscher et al.* [1998] who compare tectonic forces to decide when frontal deformation would overcome underthrusting.

[5] These force or dissipation criteria are not the outcome of mathematical theorems and should thus be used with great care, with experimental or field validation, as done by numerical means by *Del Castello and Cooke* [2007]. They could be avoided if the full solution of the boundary-valued problem was constructed by numerical means with, for example, the application of the finite element method. Results for a single thrust are found in the work of *Erickson and Jamison* [1995] and *Erickson et al.* [2001] providing insight on the orientation of a series of back thrusts for a predefined ramp. Finding the position of the ramp requires to solve a strain localization problem until a sharp discontinuity is formed. Following the thrust development over the ramp necessitates contact algorithm for finite displacement jumps. These two tasks are technically problematic and remain debated topics in an active research area, as already mentioned 20 years ago by *Platt* [1988], requiring difficult comparisons of different implementations of related formulations [*Buiter et al.*, 2006]. Moreover, one looses with the numerical codes the simplicity of analytical solutions and the possibility to conduct the thousands of iterations required for inverse methods [*Maillot et al.*, 2007].

[6] There is thus a gap between the efficient, simple geometrical constructions of thrusting, as proposed by *Suppe* [1983], and the computer-intensive mechanical solutions. These geometrical models are playing a crucial role in the interpretation of seismic sections and are applied in the industry [*Zoetemeijer and Sassi*, 1992; *Sciamanna et al.*, 2004]. One way to reconcile the mechanics approach and the geometrical constructions is to follow the steps of *Platt* [1988, 1990] and *Hardy et al.* [1998] and to accept the kinematics, proposed by the structural geologists, which then does not have to be an outcome of the mechanics problem. However, one should define a sufficient number of degrees of freedom in the kinematics (such as position and dip of faults) which could then be optimized to satisfy mechanical equilibrium and rock rheology constraints rather then be arbitrarily prescribed. This strategy was first considered for a single thrust ramp by *Maillot and Leroy* [2003] who relied on the minimum dissipation principle to orientate the back thrust. A more rigorous and general approach is offered by the application of the external approach of limit analysis [*Salençon*, 1974], classically used in soil failure analysis. A kinematically admissible (KA) velocity field is proposed and the estimated maximum internal power combined with the theorem of virtual powers leads to an upper bound in the tectonic force. The core of the method is the recognition that the stress, within the bulk material, or the stress vector, acting on discontinuities, is always within a convex domain of the stress space, referred to as the strength domain. Its boundary is, typically, the Coulomb failure criterion. This method relies on the maximum strength theorem, so-called to emphasize that only strength is involved with no appeal to a complete plasticity theory, and in particular to the flow rule. The new twist to the external approach [*Maillot and Leroy*, 2006] is that the least upper bound is not searched in the space of KA velocity fields only but in an extended space which includes the main geometrical features of the structures, which are the degrees of freedom alluded to above. These authors studied the development of a symmetric kink-fold parameterized by its amplitude. For each amplitude, their predicted geometry is the one providing the least upper bound in tectonic force. The optimized degrees of freedom are the kink dip as well as the dip of the two parallel hinges setting the kink boundary. Their selection warrants a unique kink geometry for a given amplitude. This strategy is applied here to the growth of accretionary wedges. We adopt a simple geometrical construction reminiscent of the fault-bend fold model [*Suppe*, 1983] whereby shortening results in rigid block translations along the basal décollement and the ramps. At any shortening increment we optimize the position and dips of the ramp and hinge (seen as a back thrust in this paper) of the active thrust.

[7] The paper contents are as follows. The next section presents the maximum strength theorem for the onset of thrusting first in a perfect triangular wedge, for which there is an analytical solution permitting to validate our approach, and second in a perfect wedge with a topographic perturbation which can control the position of the active thrust. The third section is devoted to the complete study of a thrust from its onset to its arrest due to the onset of a more favorable thrust accounting or not for relief buildup. It is seen that this relief leads to an increase in the upper bound in tectonic force which is inconsistent with a finite life span of the thrust. To palliate this inconsistency, a weakening of the ramp is introduced in the form of a decrease in its friction angle from an initial to a final value which leads to a decrease in the tectonic force. This decrease due to ramp weakening dominates initially over the increase due to relief buildup, resulting in a finite life span of every thrust. The fourth section presents the predictions for a normal sequence of thrusting (i.e., in the sense of *Morley* [1988], from the rear to the front within the wedge toe) ending with the prediction of the first out-of-sequence event. The fifth section is devoted to the construction of an inverse method

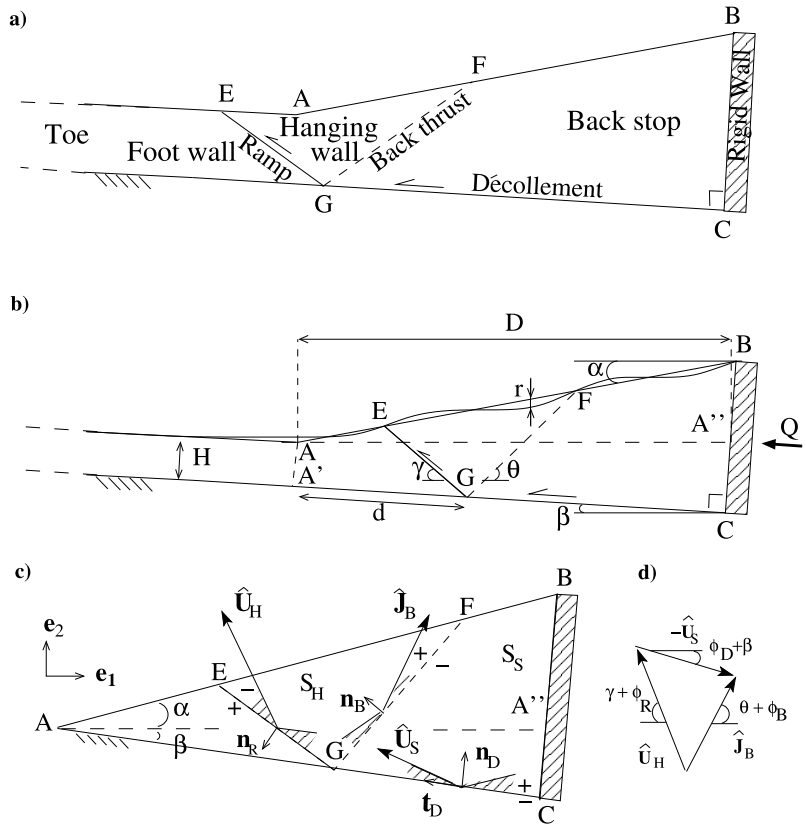


**Figure 1.** (a) The names adopted for the different regions of the accretionary wedge are defined. (b) The main mathematical symbols and variables are illustrated. Note that the top surface of the prism may have an arbitrary relief *r* measured from average the slope dipping at $\alpha$. (c) For a zero thickness toe, the wedge is triangular in shape, providing a simpler example to introduce the maximum strength theorem. (d) Compatibility of the virtual velocity field is illustrated by the hodogram which states graphically that $\hat{\mathbf{J}}_B = \hat{\mathbf{U}}_H - \hat{\mathbf{U}}_S$.

to assess the likeliness for the transfer of activity from the active to the incipient thrust in the section through the Nankai accretionary wedge corresponding to the seismic line NT62-8 studied by *Moore et al.* [1991] and by *Morgan and Karig* [1995]. The transfer requires the concomitant activity of the two structures which is marked by the same upper bound in the tectonic force. This equality of the bounds for the two structures defines the likely ranges of the initial and the final friction angles over the ramps of the incipient and active thrust, respectively. This application shows the necessity to introduce the concept of weakening to reconcile theory and observations. Strain softening, well known in the laboratory, becomes then tentatively justified at the field scale.

## 2. Onset of Thrusting Based on the Maximum Strength Theorem

[8] The main objective of this section is to present the maximum strength theorem with the help of a simple example, the onset of a thrust: a rigid back stop is sliding over a décollement up to the root of the ramp. Material in the hanging wall, separated from the back stop by the back thrust (migrating hinge), is moving up parallel to the ramp (Figure 1a). We will determine the dips $\theta$ and $\gamma$ of the back thrust and ramp, respectively, as well as the position of the base of the ramp, defined by the distance *d* from point A′ to G (Figure 1b). In this section, it is the simplified geometry of Figure 1c which is considered: the wedge is triangular in the absence of any toe.

### 2.1. Geometry, KA Velocity Field, and Equilibrium

[9] The triangular-shaped wedge occupies the region ABC in Figure 1c and defines the studied domain referenced as $\Omega$. The taper is the angle $\alpha + \beta$ where $\alpha$ corresponds to the slope of the topography and $\beta$ to the dip of the décollement. The length of the wedge is measured along the horizon $AA''$ and denoted $D$. The onset of thrusting is due to the compression by the rigid wall along segment BC perpendicular to the décollement. It results in slip of the back stop (region GFBC) over the segment GC of the décollement. Material in region EFG, defining the hanging wall, is sliding over the ramp EG. The segment GF marks a discontinuity in the velocity field which is the back thrust. It should also be seen as a migrating hinge since materials from the back stop are crossing it to reach the hanging wall. An important assumption adopted throughout the paper is that every material block undergoes rigid body motion. Thus a material point from the back stop region would be translated toward the back thrust, be sheared when crossing it, and then be translated again parallel to the ramp. (This kinematics is typical of a "push" theory. It is shown in

the auxiliary material[1] that the "pull" theory, as defined by *Dahlen and Barr* [1989] and corresponding to an immobile back wall, would lead to the same results as those presented here. This kinematics is also the simplest to construct geometrically a fold. One could envision to account for other modes of deformation and apply the same strategy in terms of optimization.) We concentrate first on the onset of thrusting. Evolution due to actual slip on the thrusts is developed in section 3. The rigid wall transmits the tectonic force $Q\mathbf{t}_D$, in which $\mathbf{t}_D$ is the unit vector tangent to the décollement and $Q$ the positive scalar for which we seek an upper bound (Figure 1c). Vectors in Figure 1c and in what follows are denoted by bold characters.

[10] The full mathematical development of the method at the center of this contribution is found in the work of *Maillot and Leroy* [2006] and based on the seminal work of *Salençon* [1974, 2002]. Only the main steps of the theory through its application to the wedge of Figure 1c are presented here for sake of conciseness.

[11] The concept of mechanical equilibrium is first appealed to with the theorem of virtual powers which states the equality between the internal and external virtual powers, two quantities which are now defined. The internal virtual power $\mathcal{P}_i$ is the power due to all gradients or discontinuities in the virtual velocity field. The virtual velocity field is any velocity field which satisfies the boundary conditions. Any such field $\hat{\mathbf{U}}$ is called kinematically admissible (KA) and is designated with a superposed hat. In agreement with the assumption of rigid body motion, we will only consider here constant KA velocity fields over each block. In this case, the internal virtual power is only performed over the velocity discontinuities, which are the ramp (EG), the back thrust (GF), and the décollement (GC). The discontinuities or interfaces are oriented by their normal $\mathbf{n}_a$, the subscript $a$ being either R, B, or D, for the ramp, the back thrust or the décollement, respectively (Figure 1c). A set of virtual velocities is illustrated in Figure 1c: the hanging wall has the virtual velocity $\hat{\mathbf{U}}_H$ and the back stop, $\hat{\mathbf{U}}_S$. The velocity discontinuity, or velocity jump, across any discontinuity, is the difference between the velocities on the positive side and on the negative side. Thus, the velocity jump across the décollement is $\hat{\mathbf{J}}_D = \hat{\mathbf{U}}_S$ since the velocity of the foot wall is zero with respect to the observer attached to the décollement. For the same reason, the velocity jump across the ramp is $\hat{\mathbf{J}}_R = -\hat{\mathbf{U}}_H$, and that across the back thrust is $\hat{\mathbf{J}}_B = \hat{\mathbf{U}}_H - \hat{\mathbf{U}}_S$. Note that these virtual velocities do not describe necessarily the actual motion of the blocks and any KA velocity field could be used in the theorem of virtual powers.

[12] If the stress vector $\mathbf{T} = \sigma\cdot\mathbf{n}_a$ ($\boldsymbol{\sigma}$ is the Cauchy stress tensor, and any second-order tensor is in bold character) was known for each discontinuity, one could readily compute the internal virtual power as the product of $\mathbf{T}$ by the velocity jump: $\hat{\mathbf{J}}\cdot\mathbf{T}$. The sum of the independent contributions of each discontinuity would then define the internal power

$$\mathcal{P}_i(\hat{\mathbf{U}}) = \int_{\Sigma_U} \hat{\mathbf{J}} \cdot \mathbf{T} dS, \tag{1}$$

in which $\Sigma_U$ denotes the set of velocity discontinuities just defined. The external virtual power

$$\mathcal{P}_e(\hat{\mathbf{U}}) = -\int_{\Omega} \rho g \mathbf{e}_2 \cdot \hat{\mathbf{U}} dV + Q\mathbf{t}_D \cdot \hat{\mathbf{U}}_S, \tag{2}$$

is due to gravity acting over the whole domain $\Omega$ (volume integral, first term on the right-hand side) and the tectonic force applied on the right boundary. In this equation, $\rho$ is the material density, assumed to be constant over the whole domain and $-g\mathbf{e}_2$ is the gravity acceleration. Note that $\{\mathbf{e}_1, \mathbf{e}_2\}$ is the orthonormal basis defined in Figure 1c. The theorem of virtual powers states that internal and external virtual powers are identical for any KA velocity field

$$\mathcal{P}_i(\hat{\mathbf{U}}) = \mathcal{P}_e(\hat{\mathbf{U}}) \quad \forall\, \hat{\mathbf{U}}\,\mathrm{KA} \tag{3}$$

Note that the main difficulty in solving (3) is that the system of stress vectors $\mathbf{T}$ acting on the discontinuities found in (1) is not known a priori. It will be seen next that one can obtain an upper bound to the internal virtual power, and therefore to the tectonic force $Q$, without ever determining this system.

### 2.2. Material Strength Domain and the Support Function

[13] The discontinuities in the velocity field and the boundary interfaces are assumed to be purely frictional. Their strength is a function of the resolved shear stress $\tau'$ and normal stress $\sigma_n'$ defined as

$$\tau' = \mathbf{t}_a \cdot \mathbf{T}', \quad \sigma_n' = \mathbf{n}_a \cdot \mathbf{T}', \tag{4}$$

in terms of the stress vector. The discontinuity can sustain any stress states found in the following Coulomb strength domain $G$ defined by

$$|\tau'| + \sigma_n' \tan\phi_a \le c_a\,, \tag{5}$$

in which $\phi_a$ and $c_a$ are the friction angle (the friction coefficient $\mu_a = \tan\phi_a$ will also be used and its value indicated between parentheses) and the cohesion of the discontinuity $a$. Such a strength domain is illustrated in Figure 2. Note that the engineering convention where $\sigma_n < 0$ in compression is used here. Equality in (5) defines the Coulomb failure criterion, i.e., the maximum strength of the discontinuity. The terminology of strength domain could be surprising to the reader accustomed to the concept of elastic regime or domain. Since no assumption concerning the rock elasticity properties is introduced, the term strength domain is found more appropriate.

[14] The next step consists of searching for the maximum internal power at every point of the fault for a given jump $\hat{\mathbf{J}}$, which is defined by

$$\varpi(\hat{\mathbf{J}}) = \operatorname*{Sup}_{\mathbf{F}Ft'\in G} \{\hat{\mathbf{J}} \cdot \mathbf{T}'\}. \tag{6}$$

Note that all $\mathbf{T}'$ in $G$ are considered in the search and no reference is made to the exact but unknown stress vector.

[1]Auxiliary materials are available in the HTML. doi:10.1029/2008JB005717.

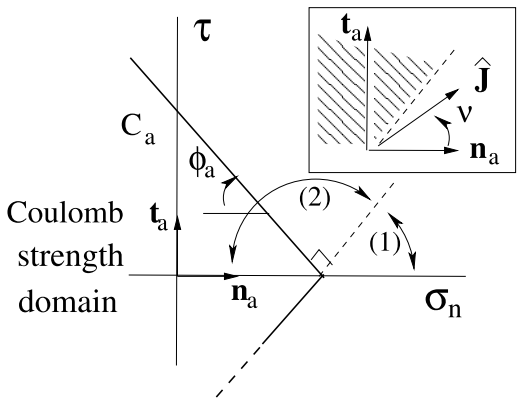


**Figure 2.** The Coulomb strength domain, the definition of the orientation of the virtual velocity jump $\hat{\mathbf{J}}$ with respect to the normal to the discontinuity in inset, and the orientation zoning for defining the support function. The $(\sigma_n,\tau)$ stress space is oriented physically with the normal $\mathbf{n}$ and the tangent $\mathbf{t}$ vectors to the discontinuity ($\mathbf{n}$, $\mathbf{t}$) direct basis. It is only if $\hat{\mathbf{J}}$ is oriented toward region 1 that the support function is finite. By symmetry of the strength domain, the same results are obtained for $\nu \leq 0$.

The maximum $\varpi(\hat{\mathbf{J}})$ exists because the strength domain is convex and contains the zero stress vector; it is called the support function in convex analysis [*Salençon*, 1974, 2002; *Maillot and Leroy*, 2006]. The orientation of the velocity jump $\hat{\mathbf{J}}$ is measured as the angle $\nu$ with the normal $\mathbf{F}Fn_a$ (inset in Figure 2). For simplicity, Figure 2 illustrates the case $0 \leq \nu \leq \pi$, but the same treatment holds for $-\pi \leq \nu \leq 0$, owing to the symmetry of the strength domain. Two cases indicated as (1) and (2) are defined by the comparison of $\nu$ with $\pi/2 - \phi_a$. The support function reads accordingly

$$\begin{aligned} &\text{case}(1) : |\nu| \leq \pi/2 - \phi_a\,, \varpi(\hat{\mathbf{J}}) = \hat{J}c_a \text{cotan}(\phi_a)\cos\nu, \\ &\text{case}\,(2) : |\nu| > \pi/2 - \phi_a\,, \varpi(\hat{\mathbf{J}}) = +\infty, \end{aligned} \tag{7}$$

for $\nu \in [-\pi;\ \pi]$. Note from (7) that there is a range of orientations in the velocity jump (case 2) which is of no interest since it does not lead to a finite upper bound. This angular range is presented as a dashed region in the inset of Figure 2c. It is also presented in Figure 1c as dashed cones for each discontinuity. The angles $\pm(\pi/2 - \phi_a)$ will be referred to as the velocity cone angles. Note that the maximum in (6) is a function only of the vector $\hat{\mathbf{J}}$ and, of course, of the strength parameters $c_a$ and $\phi_a$ defining $G$, but not of the exact unknown stress vector $\mathbf{T}$.

### 2.3. Maximum Strength Theorem and Upper Bound on the Tectonic Force

[15] The introduction of the support function (6) allows us to establish an upper bound of the internal virtual power (1) which reads

$$\mathcal{P}_i(\hat{\mathbf{U}}) \leq \int_{\Sigma_U} \underset{\mathbf{T}' \in G}{\text{Sup}} \{\hat{\mathbf{J}} \cdot \mathbf{T}'\} dS = \int_{\Sigma_U} \varpi(\hat{\mathbf{J}}) dS. \tag{8}$$

The theorem of virtual powers (3) together with the definition of the external power (2) then provide

$$Q\mathbf{t}_D \cdot \hat{\mathbf{U}}_S \leq \int_\Omega \rho g \mathbf{e}_2 \cdot \hat{\mathbf{U}} dV + \int_{\Sigma_U} \varpi(\hat{\mathbf{J}}) dS, \tag{9}$$

leading to an upper bound in the tectonic force $Q$. The best upper bound is defined as the least upper bound since it is the closest to the exact solution. It is obtained by minimizing the right-hand side of (9) seen as a function of the two virtual velocities $\hat{\mathbf{U}}_S$ and $\hat{\mathbf{U}}_H$, the two angles $\theta$ and $\gamma$, and the position $d$ of the root of the ramp and back thrust. Before proceeding to this optimization, we need an explicit expression for the upper bound (9) in terms of these variables, starting with the velocities.

[16] The first velocity vector to be discussed is the virtual velocity of the back stop. It has for norm $\hat{U}_S$ and is oriented with the velocity cone angle $\nu = \pi/2 - \phi_D$. The second virtual velocity vector is $\hat{\mathbf{U}}_H$ and is oriented such that the velocity jump across the ramp $\hat{\mathbf{J}}_R = -\hat{\mathbf{U}}_H$ has the orientation defined by the velocity cone angle ($\nu = \pi/2 - \phi_R$), to minimize work against gravity over the hanging wall. Another constraint on the norm of $\hat{\mathbf{U}}_H$ is found by imposing that the velocity jump vector across the back thrust $\hat{\mathbf{J}}_B = \hat{\mathbf{U}}_H - \hat{\mathbf{U}}_S$ is oriented with the velocity cone angle $\nu = -\pi/2 + \phi_B$. These conditions and constraints are reproduced in the hodogram presented in Figure 1d which leads to

$$\hat{U}_H = \hat{U}_S \frac{\sin(\phi_B + \phi_D + \beta + \theta)}{\sin(\phi_B + \phi_R + \gamma + \theta)}, \tag{10}$$

as well as

$$\hat{J}_B = \hat{U}_S \frac{\sin(\phi_R - \phi_D + \gamma - \beta)}{\sin(\phi_B + \phi_R + \gamma + \theta)}, \tag{11}$$

by application of the law of sines. Note that the mathematical proof that the selections of the velocity cone angle $\nu = \pi/2 - \phi_a$, for orienting the velocity jumps over the ramp and the décollement, and of the angle $\nu = -\pi/2 + \phi_B$ for the jump on the back thrust do minimize the upper bound is not provided here for sake of conciseness. This proof is the result of an exercise in optimization with constraints and is presented in the auxiliary material.

[17] The expression for the tectonic upper bound (9) is now made explicit in terms of the geometry of the triangular shaped wedge and its material properties

$$\begin{aligned} Q\cos\phi_D \leq \rho g \Bigg[ & S_H \frac{\sin(\phi_B + \phi_D + \beta + \theta)}{\sin(\phi_B + \phi_R + \gamma + \theta)} \sin(\phi_R + \gamma) \\ & + S_S \sin(\phi_D + \beta) \Bigg] \\ & + c_R \cos\phi_R \frac{\sin(\phi_B + \phi_D + \beta + \theta)}{\sin(\phi_B + \phi_R + \gamma + \theta)} L_R + c_D \cos\phi_D \\ & \cdot (D\cos\beta - d) + c_B \cos\phi_B \frac{\sin(\phi_R - \phi_D + \gamma - \beta)}{\sin(\phi_B + \phi_R + \gamma + \theta)} L_B\,, \end{aligned} \tag{12}$$

in which $S_H$, $S_S$, $L_R$ and $L_B$ denote the surface of the hanging wall, of the back stop (Figure 2c) and the length of the ramp and of the back thrust, respectively. Note that the two sides of (9) have been divided in (12) by the positive scalar $\hat{U}_S$ which is arbitrary.

### 2.4. Least Upper Bound on the Tectonic Force for a Perfect Triangular Wedge

[18] The upper bound in (12) is now minimized in terms of $d$, $\theta$ and $\gamma$ for the triangular wedge. In that case, the surfaces and length introduced in (12) are readily computed and the upper bound becomes a second-order polynomial in the normalized distance $\tilde{d}$ defining the position of the root of the thrust

$$\begin{aligned}
&\tilde{Q}(\theta,\gamma,\tilde{d}) \le Q_1 + Q_2(\theta,\gamma)\tilde{d} + Q_3(\theta,\gamma)\tilde{d}^2 \\
&\text{with} \quad Q_1 = \frac{1}{2}\frac{\cos^2\beta\tan(\alpha+\beta)\sin(\phi_D+\beta)}{\cos\phi_D} + \cos\beta\,\tilde{c}_D\,, \\
&Q_2(\theta,\gamma) = -\tilde{c}_D + \frac{\sin(\alpha+\beta)}{\cos\phi_D\sin(\phi_B+\phi_R+\gamma+\theta)} \\
&\qquad \cdot\left[\frac{\cos\phi_R}{\sin(\alpha+\gamma)}\sin(\phi_B+\phi_D+\beta+\theta)\tilde{c}_R\right. \\
&\qquad \left. + \frac{\cos\phi_B}{\sin(\theta-\alpha)}\sin(\phi_R-\phi_D+\gamma-\beta)\tilde{c}_B\right], \\
&Q_3(\theta,\gamma) = \frac{\sin(\alpha+\beta)}{2\cos\phi_D\sin(\theta-\alpha)}\left[-\sin(\phi_D+\beta)\sin(\beta+\theta)\right. \\
&\qquad + \frac{\sin(\alpha+\beta)\sin(\theta+\gamma)}{\sin(\alpha+\gamma)} \\
&\qquad \left. \cdot\sin(\phi_R+\gamma)\frac{\sin(\phi_B+\phi_D+\beta+\theta)}{\sin(\phi_B+\phi_R+\gamma+\theta)}\right],
\end{aligned} \tag{13}$$

in which the superposed ˜ designates dimensionless quantities which are obtained by dividing lengths and stress-like quantities by the reference length $D$ and the stress $\rho g D$, respectively. The scalar $Q_1$ in (13) is due to work done against gravity (for the whole structure of characteristic length $D$) and the work done along the segment $GC$ of the décollement cohesion. It is independent of the angles $\theta$ and $\gamma$. The scalar $Q_2$ in (13) is due to the cohesion of the interfaces and discontinuities since the internal power is then proportional to the length of these lines. The last scalar $Q_3$ is due to gravity and thus associated to the square of $\tilde{d}$.

[19] The least upper bound is obtained by minimizing $\tilde{Q}(\theta, \gamma, \tilde{d})$ in terms of its three arguments, an exercise done by numerical means in this paper. However, for the particular expression in (13), and letting $Q_2$ vanish by assuming no cohesion along the interfaces and discontinuities, the critical $\tilde{d}$ is readily obtained analytically. It depends on the sign of $Q_3$. If positive, the best candidate is 0. If negative, $\tilde{d}$ takes the maximum value consistent with the rooting of the ramp and the back thrust on the décollement. All values of $\tilde{d}$ are admissible if $Q_3 = 0$. This particular solution, computed by numerical means for the optimum $\theta$ and $\gamma$, is compared to the exact Rankine solution proposed by *Dahlen* [1984] and constructed geometrically by *Lehner* [1986], in Figure 3. The orientation of the ramp is exactly given by

$$\gamma = \frac{1}{2}\arcsin\left(\frac{\sin\alpha}{\sin\phi_R}\right) + \frac{\alpha}{2} + \frac{\pi}{4} - \frac{\phi_R}{2}, \tag{14}$$

and the dip of the back thrust is simply the conjugate orientation (if the same friction coefficient is assumed, $\phi_B = \phi_R$). Our solutions in Figure 3a coincide within numerical accuracy to this exact solution. For a zero slope $\alpha$, the orientation is the classical $\pi/4-\phi_R/2$. For increasing $\alpha$, the dip of the ramp decreases. These results are plotted for three different values of the ramp friction angle. Each set of curves terminates as the optimum value of $d$ shrinks to zero, corresponding to the activation of the whole décollement. This transition is found to occur as $Q_3$ is zero, for a critical $\alpha_c$ which is compared to the implicit solution proposed by *Dahlen* [1984]

$$\alpha_c + \arcsin\left(\frac{\sin\alpha_c}{\sin\phi_R}\right) = -2\beta + \arcsin\left(\frac{\sin\phi_D}{\sin\phi_R}\right) - \phi_D, \tag{15}$$

in Figure 3b for $\phi_D = 15°$ (0.27). Note again the complete agreement between our numerical solution and the exact one for three different values of the ramp friction angle. This comparison validates the numerical approach for the optimization to be used throughout this paper.

[20] This comparison with *Dahlen*'s [1984] solution gives us the opportunity to define some of the terminology used in this paper and illustrated in Figure 3b. First, we are interested in compressional deformation and the wedge is said to be critical if the taper ($\alpha + \beta$) is Dahlen's solution. For smaller angles, the taper is said to be subcritical and the deformation takes place to the rear of the wedge. For larger tapers, the conditions are said to be supercritical and the whole décollement is fully activated. Consequently, the domain of stability defined by *Dahlen* [1984], with no internal deformation in the wedge, corresponds to supercritical conditions in this paper.

[21] The last item of discussion is the influence of the material cohesion on the critical slope $\alpha_c$. The décollement cohesion is still set to zero but the back thrust and the ramp cohesions are varied from zero to $0.035\rho g D$. Results, presented in Figure 4, exhibit a sharp decrease of the critical slope $\alpha_c$ with the increase in cohesion. The more cohesive the material is, the smaller is the slope necessary to trigger the activation of the whole décollement. These results, obtained by numerical means by minimizing $\tilde{Q}$ are complemented by the following interpretation of equation (13). Coefficient $Q_2$ is always positive since $c_D$ is set to zero. If $Q_3$ is positive or null, the $\tilde{Q}$ function is monotonically increasing, its smallest value reached for $d = 0$. The wedge is supercritical. For $Q_3$ negative, the $\tilde{Q} - d$ curve is parabolic. The maximum is between $d = 0$ and $d = D \cos\beta$, disregarding geometrical constraints on the back thrust for sake of simplicity, and for sufficiently small, negative values of $Q_3$. There is a critical value of $Q_3 = -Q_2(D\cos\beta)$ for which the load $\tilde{Q}$ is identical at $d = 0$ and $d = D\cos\beta$. For even smaller value of $Q_3$, the load is the smallest at $d = D\cos\beta$. The wedge is then subcritical. The critical conditions are thus now defined not for $Q_3 = 0$, for cohesionless materials, but for $Q_3 = -Q_2(D\cos\beta)$ in the presence of cohesion. However, the transition is marked in the presence of cohesion with failure to the front and to the back but not at an arbitrary position within the bulk. The introduction of cohesion thus suppresses the arbitrary position of the failure mechanism for critical taper conditions.

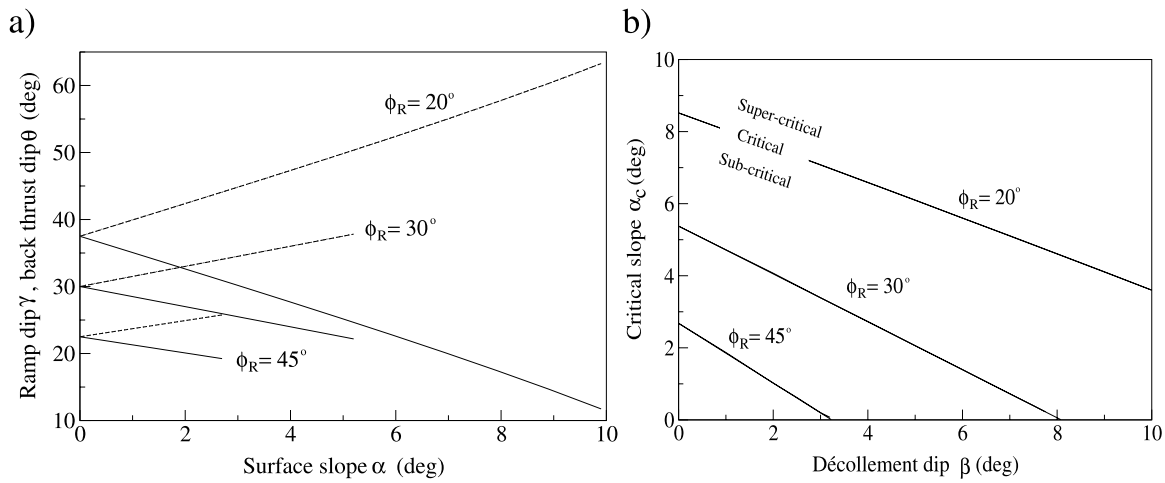


**Figure 3.** Comparison of the solution for the least upper bound and the exact solution of *Dahlen* [1984] for various ramp friction angles ($\phi_R$) and for basal friction $\phi_D$ = 15° (0.27). (a) The dips of the ramp ($\gamma$, solid lines) and of the back thrust ($\theta$, dashed lines) are presented as functions of the surface slope. (b) The critical value of the slope is presented as a function of the dip of the décollement $\beta$. In all cases, the exact and numerical solutions superpose within plotting accuracy.

### 2.5. Imperfection Analysis of the Triangular Wedge

[22] A second approach is now considered to suppress the arbitrary position of the failure mode for critical taper conditions. It consists of the introduction of an imperfection in the topography. Consider a triangular zone of relief with summit point $P$ at the distance $\eta_P$ from the top surface (set to an arbitrary 440 m here, with $D$ = 100 km, $\beta$ = 0°). The slope of the triangle is set to 10° with respect to the wedge surface. Point P is at the distance $\xi_P$ from the tip of the wedge (Figure 5a).

[23] Results will be interpreted as the competition between two major failure modes. Mode 1 consists of the activation of the whole décollement, typical of supercritical wedges. Failure in mode 2 is at the rear and is typical of subcritical wedges, the ramp either cutting through or not cutting through the imperfection, as illustrated in Figure 5c. The activated sections of the décollement and the ramp are in thick solid line; the back thrusts are depicted as dashed lines. A third mode is also introduced and results from the competition between the two first modes and is defined by the locking of the thrust on the imperfection. There are two variants labeled 3′ and 3″ for which the ramp and the back thrust are locked at the back or the front of the imperfection, where the slope is discontinuous, respectively.

[24] The range of surface slope $\alpha$, for which the length $\tilde{d}$ is neither zero nor maximum, is presented as a function of the position $\tilde{\xi}_P(= \xi_P/D)$ of the imperfection in Figure 5b. This range is called the imperfection locking range in this section and corresponds to the regions labeled 3′ and 3″ in the graph. Consider for example $\xi_P$ set to 20 km ($\tilde{\xi}_P$ = 0.2). The locking range in $\alpha$ has for lower and upper limits $\alpha_c$ = 5.38° and 5.6°, respectively. For $\alpha$ larger then the upper limit, the whole décollement is activated: failure mode 1 dominates and the wedge is supercritical. Below that upper limit, there is competition between failure modes 1 and 2, resulting in the variant 3′. The more to the front is the imperfection, smaller values of $\tilde{\xi}_P$, the longer is the length of the décollement activated and the larger is the locking range. The lower limit in the locking range is $\alpha_c$, for any perturbation position less than 72 km from the tip of the wedge toe. For $\alpha$ smaller than $\alpha_c$, the failure mode is of type 2, at the back of the wedge which is then subcritical. For imperfection positions $\xi_P$ larger than this critical value of 72 km, the upper limit of the locking range is constant, 5.375°, so slightly lower than $\alpha_c$. The lower limit decreases with increasing $\tilde{\xi}_P$. The interpretation is as follows. For $\alpha$ larger than the upper limit, the whole décollement is activated corresponding to failure mode 1, typical of a supercritical wedge. Note that the imperfection contributes to the weight of the thrusting section of the wedge, explaining the slight difference in the upper limit from $\alpha_c$. For $\alpha$ smaller than

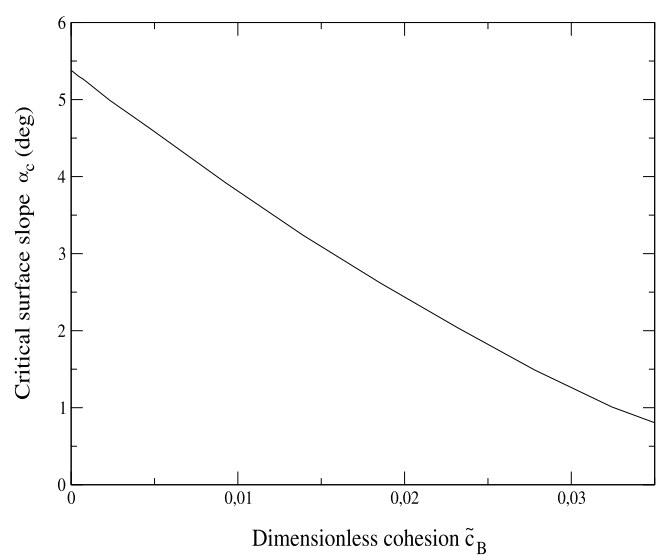


**Figure 4.** Influence of the cohesion of the ramp and back thrust ($c_B = c_R$, $c_D$ = 0), on the critical slope.

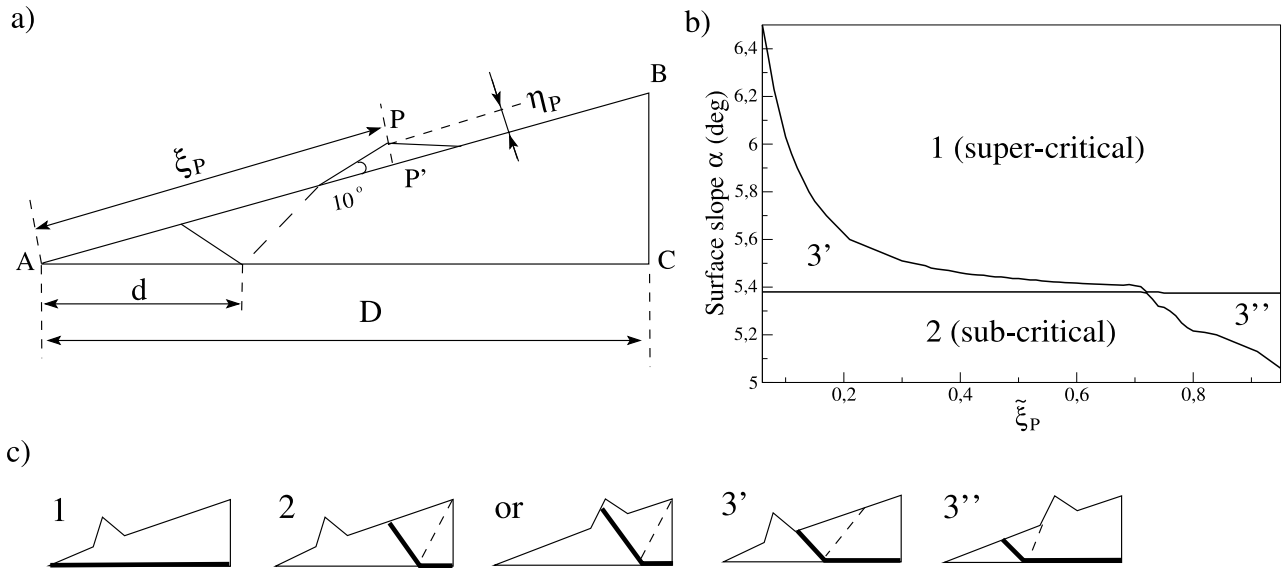


**Figure 5.** Imperfection analysis for the triangular wedge. (a) The asperity geometry is presented with the distance $\xi_P$ defined as the distance $AP'$. (b) The locking range of the imperfection in slope $\alpha$ is function of the imperfection position $\xi_P$. (c) Three modes of failure are defined: full décollement activated for a supercritical wedge (mode 1); deformation to the rear, typical of a subcritical wedge (mode 2); and the locking mode, with two variants (modes 3′ and 3″). They correspond to the ramp or the back thrust outcropping at the rear or to the front of the imperfection, respectively.

5.375°, the wedge ceases to be supercritical, the variant 3″ is then observed and the imperfection is thus locking the thrust. The lower limit in the locking range marks the onset of the dominance of mode 2, typical of subcritical wedges. Note that the locking range as well as the critical distance of 72 km are functions of the imperfection mass and thus of the height $\eta_P$. Repeating the analysis for smaller $\eta_P$'s reveals that the locking range tends to a single point $\alpha_c$.

[25] This simple example has at least two merits. First, it shows the potential of the proposed methodology in the absence of analytical solutions. Second, it reveals that minute changes in the topography of the top surface could lead to drastic changes in the position of the active ramp within the wedge if close to criticality.

## 3. Thrust Folding Based on the Maximum Strength Theorem

[26] The objective of this section is to discuss the evolution of a thrust starting with the simple case where the top surface and the décollement have a zero slope. The initial distance of the ramp to the back stop is then arbitrarily set to $D$.

[27] It is first assumed that erosion is fast such that no relief builds up despite the shortening of the back stop (Figure 6a). This simple geometry permits investigation of the influence of the ramp friction coefficient on the orientation of the back thrust and is reminiscent of the example treated by *Maillot and Leroy* [2003] and *Maillot et al.* [2007]. The second example disregards erosion and the relief is constructed assuming the hanging wall glides rigidly over the ramp, except for the material forming the forelimb (Figure 6b). The relief $r$ is such that the surface area is preserved during compression. Material and geometrical parameters are summarized in Table 1 (third column). Note that all cohesions are set to zero in what follows.

### 3.1. A Simple Thrust Fold With Fast Erosion

[28] This example is proposed to test the influence of the friction angle over the ramp. This angle is either kept constant during thrusting or chosen to decrease linearly from an initial value $\phi_{Ri}$ to the final value $\phi_{Rf}$ after a transition defined by the distance $\delta_T$, in accumulated displacement over the ramp $\delta_R$ (Figure 6c). Note that the friction angle of the back thrust is always kept constant, equal to the friction angle of the pristine, bulk material, because the material within the back thrust is displaced from the back stop toward the hanging wall with no time to sustain the damage occurring over the ramp by the residing material. This difference is essential to justify the different treatment adopted for the friction angles of the ramp and the back thrust during evolution. Note also that softening could have been also introduced on the material cohesion or on both the cohesion and the friction angle. These alternative approaches could be of interest if one has experimental results on the analogue material properties and desires to apply the inverse method presented in section 5 to laboratory experiments, such as those of *Lohrmann et al.* [2003]. Simplicity guides us in selecting the linear softening construction on the friction angles.

[29] The geometry of the hanging wall during the evolution remains unchanged, except for the shortening: material points in the back stop are first displaced horizontally by $\delta$, cross the back thrust GF, then move in the hanging wall parallel to the ramp and are eroded away at their arrival on

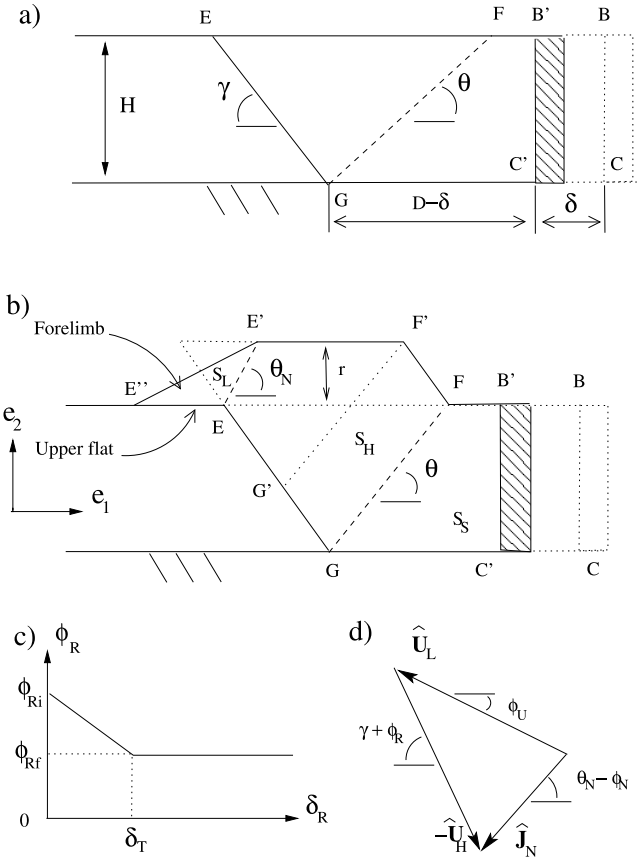


**Figure 6.** The first two examples of evolution concern a thrust initiating from a layer of thickness $H$ (the angles $\alpha$ and $\beta$ of Figure 1 are zero). (a) Erosion is fast such that no relief builds up. (b) The relief is composed of the plateau $E'F'$ and a forelimb, the latter corresponding to the collapse of the tip of the hanging wall over the upper flat. (c) The friction coefficient over the ramp decreases from an initial value $\phi_{Ri}$ to the final value $\phi_{Rf}$ after a displacement of $\delta_T$. (d) The hodogram for the velocity jumps of the discontinuity associated with the forelimb is presented.

segment EF. This similarity of the geometries means that the upper bound in tectonic force is still given by (12) in which lengths and surfaces take simple expressions leading to

$$\begin{aligned}\tilde{Q}\cos\phi_D \le{}& \frac{\tilde{H}^2}{2}(\operatorname{cotan}\gamma + \operatorname{cotan}\theta)\frac{\sin(\phi_B+\phi_D+\theta)}{\sin(\phi_B+\phi_R+\gamma+\theta)}\\ &\cdot \sin(\phi_R+\gamma) + \tilde{H}\left(1-\tilde{\delta}-\frac{\tilde{H}}{2}\operatorname{cotan}\theta\right)\\ &\cdot \sin\phi_D + \tilde{c}_R\cos\phi_R\frac{\sin(\phi_B+\phi_D+\theta)}{\sin(\phi_B+\phi_R+\gamma+\theta)}\frac{\tilde{H}}{\sin\gamma}\\ &+ \tilde{c}_D\cos\phi_D(1-\tilde{\delta}) + \tilde{c}_B\cos\phi_B\frac{\sin(\phi_R-\phi_D+\gamma)}{\sin(\phi_B+\phi_R+\gamma+\theta)}\\ &\cdot\frac{\tilde{H}}{\sin\theta}. \end{aligned} \tag{16}$$

The least upper bound in force (16) based on the optimum orientation of the back thrust is presented in Figure 7a for different values of the final friction angle $\phi_{Rf}$. The dashed line shows that for a constant friction coefficient over the ramp, the upper bound in tectonic force decreases linearly with increasing $\tilde{\delta}$, as seen from (16). This is due simply to the erosion of the mass of the relief created during the thrusting event. This decrease is magnified if the activation of the ramp leads to a reduction in its friction angle. Note that once the final friction angle is reached the evolution of the three solutions are parallel for the reason discussed above. Note also that according to (16), the shortening of the décollement (first term in third line) should also lead to a reduction in the upper bound. This influence is however not felt here since all cohesions are set to zero (Table 1, third column). Attention is now centered on the influence of the reduction in the friction coefficient on the variation of the orientation of the optimum back thrust. This influence is analyzed from the results presented in Figure 7b: the back thrust dip varies from 30° to 45° for a $\phi_{Rf}$ of 10° (0.18). Note that once the ramp weakening ceases, the back thrust dip remains constant, showing that it is independent of the extent of the back stop, as predicted by *Maillot and Leroy* [2003].

**Table 1.** Definition of Parameters and Their Values or Ranges for the Study of the Single Thrust With Fast Erosion or Relief Buildup in Section 3 and of the Sequence of Thrusting in Section 4[a]

| Symbol | Definition | Value (Single) | Value (Sequence) | Unit |
|---|---|---|---|---|
| $\alpha$ | topographic initial slope | 0 | [4.5°; 7.5°] | deg |
| $\beta$ | slope of décollement and | 0 | [0°; 3°] | deg |
| $\phi_B$ | friction angle of bulk and back thrust | 30° (0.58) | 30° (0.58) | deg |
| $\phi_D$ | friction angle of décollement | 15° (0.27) | [5° (0.09); 15° (0.27)] | deg |
| $\phi_{Ri}$ | initial friction angle of the ramp (= $\phi_B$) | 30° (0.58) | 30° (0.58) | deg |
| $\phi_{Rf}$ | final friction angle of the ramp | [10° (0.18); 30° (0.58)] | [15° (0.27); 25° (0.47)] | deg |
| $\phi_N$ | friction angle of normal fault (= $\phi_B$) | 30° (0.58) | 30° (0.58) | deg |
| $\phi_U$ | friction angle of the upper flat ( = $\phi_D$) | 15° (0.27) | [5° (0.09); 15° (0.27)] | deg |
| $c_a$ | cohesions ($a$ = $R$, $U$, $D$, $B$ and $N$) | 0 | 0 | MPa |
| $\delta_T$ | displacement transition from $\phi_{Ri}$ to $\phi_{Rf}$ | 0 or 2 | [0; $D$/50] | km |
| $H$ | thickness of toe | 1 | 1 | km |
| $D$ | length of prism | 100 | 100 | km |
| $\rho$ | mass density | 2200 | 2200 | kg/m$^3$ |
| $g$ | gravity acceleration | 9.81 | 9.81 | m/s$^2$ |

[a]The third column shows the single thrust with fast erosion or relief buildup and the fourth column shows the sequence of thrusting. The subscripts B, D, N, R, U stand for the bulk or back thrust, the décollement, the normal fault bounding the forelimb, the ramp, and the upper flat, respectively. The friction properties are defined in terms of angle $\phi_a$ and coefficient (tan $\phi_a$) in parentheses.

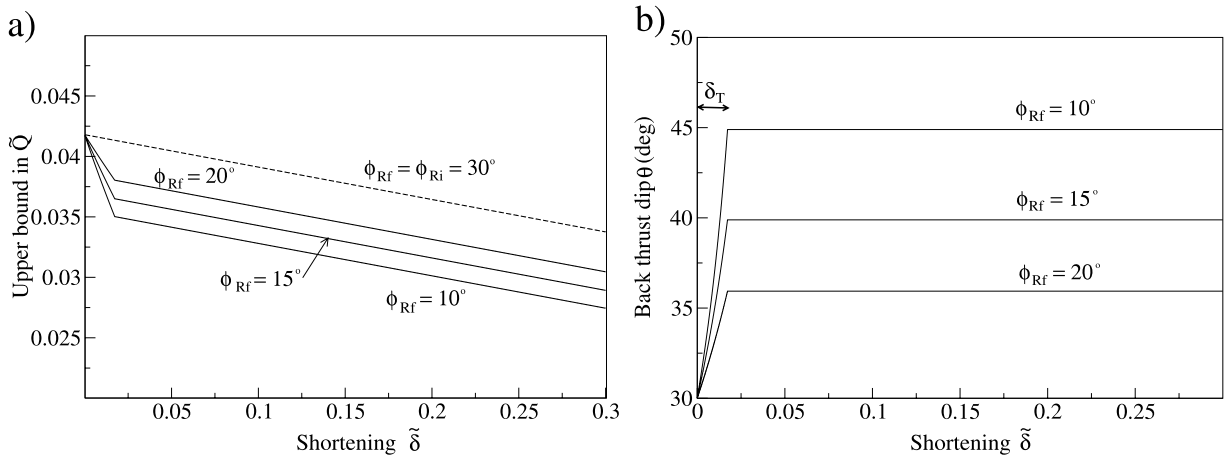


**Figure 7.** (a) The upper bound in tectonic force and (b) the optimum orientation of the back thrust as functions of the shortening for the case of thrusting with fast erosion, presented in Figure 6a. Different values of the final friction angle of the ramp $\phi_{Rf}$ are considered. The variation in friction angle from the initial value $\phi_{Ri} = 30°$ (0.58) occurs over a displacement of $\delta_T = 2$ km, a large value selected for sake of clarity of the graphs.

### 3.2. A Simple Thrust Fold With Relief Buildup

[30] Erosion is now disregarded and the relief, measured by the distance $r$, builds up in response to the shortening of the back stop by $\delta$ (Figure 6b). Section GCBF is transformed in section GC′B′F and is accompanied by the thrusting of section GEF so that points initially along GF are now on G′F′. The hanging wall has been translated rigidly except for the material now in section EE′E″ which has been projected on the upper flat (interface labeled $U$). Constant frictional properties are assigned to the upper flat, chosen to be identical to the décollement for sake of simplicity. The forelimb is separated from the hanging wall by a normal fault dipping at $\theta_N$ and corresponding to the segment $EE'$. This normal fault is a migrating hinge, as the back thrust, and is assumed to have the same properties as those of the bulk material. The length of the upper flat $L_U$ (distance E″E) is found by conservation of the part of the hanging wall surface now forming the forelimb. This projection of the hanging wall on the upper flat is of course very simple and inspired by numerous kinematic scenarios although different from the classical construction of *Suppe* [1983]. It could be amended to describe better specific field cases.

[31] The virtual velocity field to be considered for the hanging wall and the back stop is identical to the one of the first example. The new section EE′E″, defining the forelimb, has the velocity $\hat{\mathbf{U}}_L$ with magnitude found with the hodogram presented in Figure 6d. The velocity $\hat{\mathbf{U}}_L$ is oriented with the velocity cone angle condition ($\phi_U - \pi/2$) over the upper flat. Knowing the velocity $\hat{\mathbf{U}}_H$ of the hanging wall, the jump $\hat{\mathbf{J}}_N = \hat{\mathbf{U}}_L - \hat{\mathbf{U}}_H$ over the normal fault is then oriented at $\theta_N - \phi_N$ to be along the velocity cone, providing the constraint necessary to define the magnitude of $\hat{\mathbf{U}}_L$ and thus the jump magnitude

$$\hat{U}_L = \hat{U}_H \frac{\sin(\theta_N - \phi_N + \gamma + \phi_R)}{\sin(\phi_U + \theta_N - \phi_N)},$$
$$\hat{J}_N = \hat{U}_H \frac{\sin(\gamma + \phi_R - \phi_U)}{\sin(\phi_U + \theta_N - \phi_N)}. \quad (17)$$

The maximum strength theorem then provides the following upper bound

$$\begin{aligned}\tilde{Q}\cos\phi_D \le{}& \tilde{S}_L \sin\phi_U \tilde{U}_L + \tilde{S}_H \sin(\gamma+\phi_R)\tilde{U}_H + \tilde{S}_S \sin\phi_D \tilde{U}_S \\ &+ \tilde{c}_U \cos\phi_U \tilde{L}_U \tilde{U}_L + \tilde{c}_N \cos\phi_N \tilde{L}_N \tilde{J}_N + \tilde{c}_R \cos\phi_R \tilde{L}_R \tilde{U}_H \\ &+ \tilde{c}_B \cos\phi_B \tilde{L}_B \tilde{J}_B + \tilde{c}_D \cos\phi_D \tilde{L}_D, \quad (18)\end{aligned}$$

in which all virtual velocities ($\tilde{U}_a = \hat{U}_a/\hat{U}_S$) are obtained by normalization with the arbitrary back stop velocity. Surfaces $S_a$ are defined in Figure 6b. The lengths $L_U$, $L_N$, $L_R$, $L_B$, and $L_D$ correspond to the lengths of segment EE″, EE′, EG, GF, and GC′ on Figure 6b. This upper bound needs to be minimized in terms of the three angles $\theta$, $\gamma$, and $\theta_N$ with a clear dependence of the morphology of the thrust on the history of these angles. This minimization is discussed next.

[32] The dip of the normal fault $\theta_N$ affects the length $L_U$ of the upper flat, the surface $S_L$ of the forelimb and thus the current surface $S_H$. The minimization in terms of $\theta_N$ concerns terms in (18) which are due to gravity and cohesion over the fault and the upper flat. The latter two are likely to be negligible once the relief $r$ is important and for this reason the rest of the reasoning is based on cohesionless discontinuities. In that instance, the dip $\theta_N$ is found by minimizing the work against gravity for the forelimb and the hanging wall which reads

$$\frac{\sin(\gamma+\theta_N)}{\sin\theta_N}\left[\sin\phi_U \frac{\sin(\theta_N - \phi_N + \gamma + \phi_R)}{\sin(\phi_U + \theta_N - \phi_N)} - \sin(\gamma+\phi_R)\right]. \quad (19)$$

It is independent of the value of $r$ which means that the forelimb will grow homotheticaly during thrusting. The angle $\theta_N$ is thus constant as long as the cohesions over the normal fault and the upper flat are disregarded.

[33] The second angle to be discussed is the dip of the ramp $\gamma$. It is assumed that the ramp detected at the onset is used throughout the evolution and the dip $\gamma$ is kept constant. One could check the validity of that assumption by com-

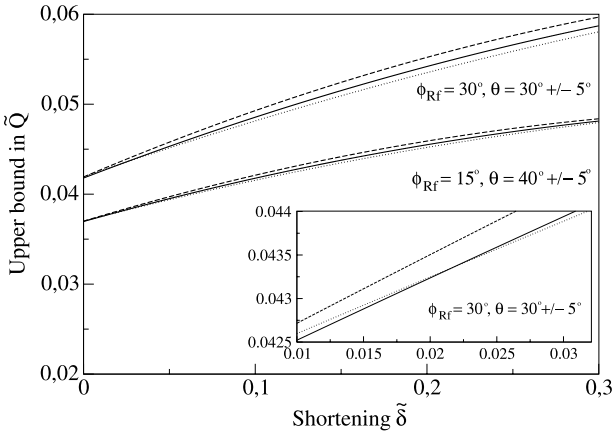


**Figure 8.** The upper bound in tectonic force as a function of dimensionless shortening $\tilde{\delta}$ for the thrusting event presented in Figure 6b. The force is increasing with shortening if relief builds up. A change in the initial optimum orientation of the back thrust by plus (dashed curves) or minus (dotted curves) 5° has little influence in the magnitude of the force. However, the optimum orientation is indeed reduced by 5° for $\tilde{\delta}$ = 0.022, as marked by the intersection of the two curves in inset.

puting the least upper bound for a different orientation. This is the strategy that will be considered in the next section revealing that it is the root of the ramp which could change during the evolution, marking the end of the thrust we are studying. The third and last angle is $\theta$, the dip of the back thrust. The first thrust analysis with erosion has shown that $\theta$ increases if the ramp friction angle decreases. The building of a relief implies more weight on the ramp and this is similar to the increase of the ramp friction angle which leads $\theta$ to decrease. This angle could thus have a complex history during thrusting with consequences on the shape of the curve FF′, drawn as a straight segment in Figure 6b. To avoid resolving this complexity, the following strategy is adopted. First, the transition distance $\delta_T$ is assumed small compared to the characteristic size of the structure $D$ and set to zero for simplicity. Consequently, the onset of the relief development is optimized in two steps. First, the ramp dip $\gamma$ is selected for the friction angle $\phi_{Ri}$. Second, the back thrust dip $\theta$ is optimized for $\phi_{Rf}$. Moreover, the angle $\theta$ is set constant to this initial value. A parametric study is now presented to shed light on the influence of the value of $\theta$ on the upper bound in tectonic force and thus to validate our optimization strategy.

[34] The results are presented in Figure 8 ($\phi_{Rf}$ set to 30° or 15°, thick solid lines). The upper bound in tectonic force in the presence of relief are increasing functions of the amount of shortening, thin solid lines, starting at the same load as for the two solutions with erosion. The dashed and dotted lines are obtained for values of $\theta$ increased or decreased by 5° with respect to the optimum value found at the onset, respectively. Two observations are in order. First, the solid line crosses the dotted line for a $\tilde{\delta}$ of 0.022, see inset of Figure 8, showing that the optimum $\theta$ has the tendency to decrease during relief buildup, as foreseen above. Second, the change by plus or minus five degrees of the back thrust orientation has little influence on the value of the upper bound, justifying the geometrical simplifications proposed here.

[35] To conclude this section, we have presented the kinematics for relief buildup and the theory necessary to determine the dips of the ramp, the forelimb normal fault and the back thrust of the first thrust. The first angle is based on the initial friction angle of the ramp $\phi_{Ri}$ (heritage from the onset) while the third is a function of the final angle $\phi_{Rf}$ (rapid rotation of the back thrust beyond the onset since $\delta_T \ll D$). The weakening ($\phi_{Ri} > \phi_{Rf}$) is attached to the ramp only and not the back thrust since material there is renewed due to the convection from the back stop to the hanging wall. The weakening will be shown to be fundamental for each thrust of a sequence to have a finite life span. The relief is composed of a forelimb separated from the hanging wall by a normal fault, which dip $\theta_N$ is found by a local minimization of the upper bound and set constant during the evolution. The upper bound in tectonic force can thus be estimated throughout the life of the thrust development and can be compared to the force necessary to initiate any new thrust. This strategy is applied in the next section to study sequences of thrusting.

## 4. Sequence of Thrusting

[36] This first objective of this section is to study the life of a single thrust from its onset, through its development to its arrest due to the onset of the next thrust. The main question is the position of the second thrust compared to the first depending on material and geometrical parameters. The second objective is to study normal sequences of thrusting until the first out of sequence event is detected. A sensitivity analysis of our predictions to the material and geometrical parameters is also included. Their values or ranges of values are summarized in Table 1 (fourth column). Note that the geometry of the thrusting sequences becomes sufficiently complex to render analytical solutions cumbersome. A numerical scheme has thus been favored and is described in Appendix A which provides also the general expression for the upper bound for thrust development with arbitrary topography.

### 4.1. Life of the First Thrust

[37] Figure 9 illustrates the influence of the initial surface slope $\alpha$ on the life of the first thrust and the position of the second thrust. The dotted lines indicate the initial topography of the toe of the wedge, and the position of the first ramp and back thrust. This initial geometry is the result of the optimization of the upper bound at the onset. The solid lines mark the topography at the end of the life of the first thrust and the dashed lines define the second thrust. The lifetime of the first ramp is estimated by the distance between the solid and dotted lines, parallel in the undisturbed region of the slope. Note that the critical slope for $\phi_{Ri} = \phi_B = 30°$ (0.58) is $\alpha_c = 5.4°$, this critical value being selected for the results presented in Figure 9c. Note that the concept of critical slope is used here and should be understood in the sense of a critical wedge keeping in mind that $\phi_B$ and $\beta$ are kept constant in this parametric study.

[38] Three observations are now in order. First, the lifetime of the first thrust would be zero in the absence of weakening on the ramp because of the increase in tectonic

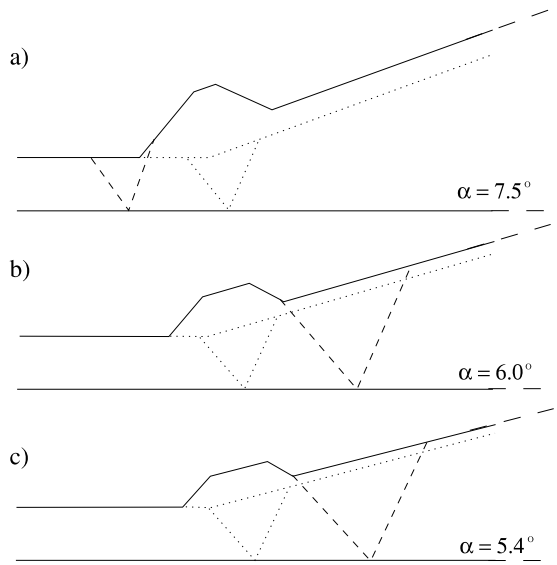


**Figure 9.** The life of the first thrust from its onset to the onset of the next thrust for three values of the surface slope $\alpha$. The dotted lines represent the initial relief, ramp and back thrust. The solid lines define the actual relief at the time of the onset of the new ramp, represented by dashed lines. The friction angles are $\phi_D = 15°$ (0.27) and $\phi_{Rf} = 15°$ (0.27). The décollement is horizontal, $\beta = 0°$. The vertical distances are scaled by a factor of 1.4.

force during relief buildup. A new optimum thrust would be detected infinitesimally close to the one just activated as soon as the first amount of relief is constructed. Second, the lifetime of the first ramp decreases substantially for decreasing $\alpha$. Third, the second thrust is out of sequence for the two lowest values of $\alpha$. For the first example (Figure 9a), the slope is larger than $\alpha_c$ and the wedge remains supercritical. The last two observations are direct consequences of the need for the topographic slope to remain everywhere close to its critical value, a qualitative concept used by *Platt* [1988] that now appears as a quantitative outcome of the optimization. These three results could be interpreted thanks to the imperfection analysis of section 2.5. The first thrust produces the relief which should be now interpreted as an imperfection close to the toe ($\xi_P \ll D$, the left of Figure 5b is of interest). For the angle $\alpha = 7.5°$, the wedge is supercritical and failure mode 1 dominates (region 1 of Figure 5b), ending with a thrust in the horizontal section of the toe. For $\alpha = 6°$, the imperfection is locking the thrust at its rear and we are in region 3′ of Figure 5b. The lower boundary of this locking range is set by $\alpha_c$, as illustrated by Figure 9c.

[39] The effect of weakening on the ramp is illustrated in Figure 10 for two values of the slope $\alpha$. These two values were selected such that the second thrusting is either in normal or out of sequence for the reasons discussed above. Initial topography and first thrust system are indicated by the solid lines. The dotted, dashed, and dotted-dashed lines show the topographies at the onset of the second thrusting for three amounts of weakening $\phi_{Ri}-\phi_{Rf}$ set to 5° (0.09), 10° (0.18) or 15°(0.27), respectively ($\phi_{Ri} = 30°$ (0.58)). The two graphs in Figures 10b and 10d show the upper bounds in $\tilde{Q}$ as a function of shortening $\tilde{\delta}$ for the first ramp with the different weakening (same style of curves as in Figures 10a and 10c) and for the onset of the second ramp with friction angle $\phi_{Ri}$ (solid curve). For any shortening $\tilde{\delta}$, two values of

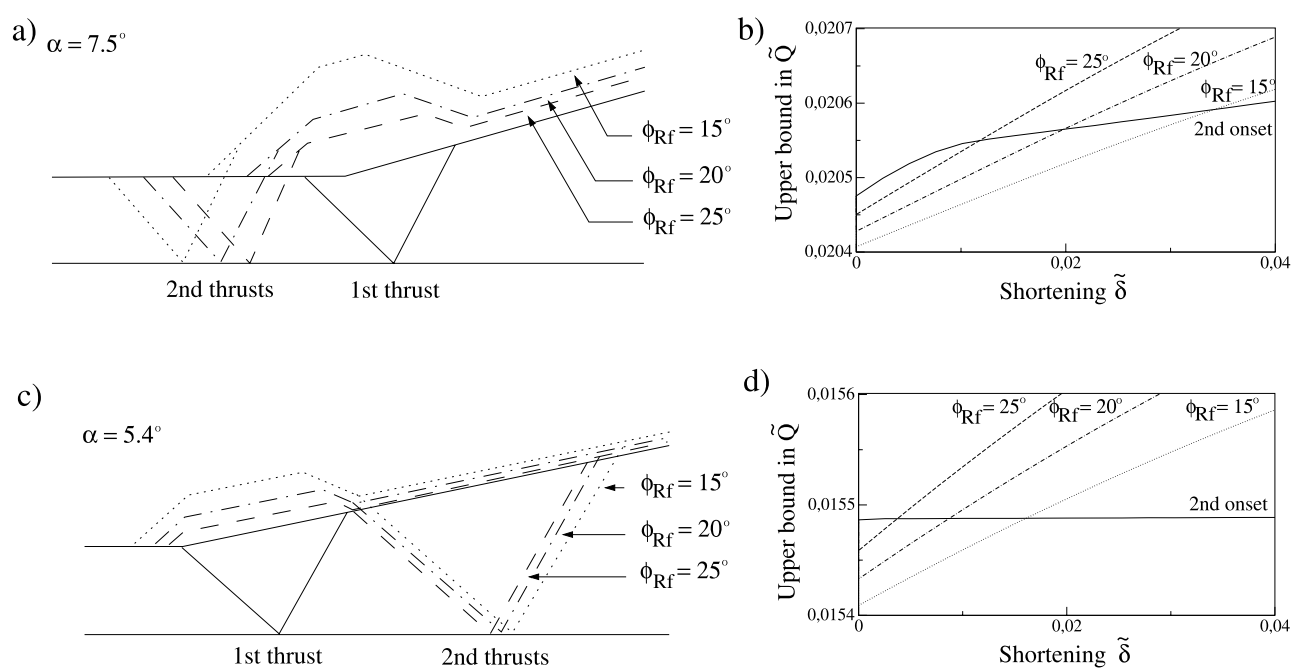


**Figure 10.** (a and c) The influence of ramp final friction angle $\phi_{Rf}$ on the life span of the first thrust and the position of the second thrust for two values of the free surface slope $\alpha$. (b and d) The predictions are based on the comparison of the various bounds in tectonic forces as a function of the shortening. The décollement is flat ($\beta = 0°$) and its friction angle is set to $\phi_D = 15°$ (0.27). The vertical distances are scaled by a factor of 1.4.

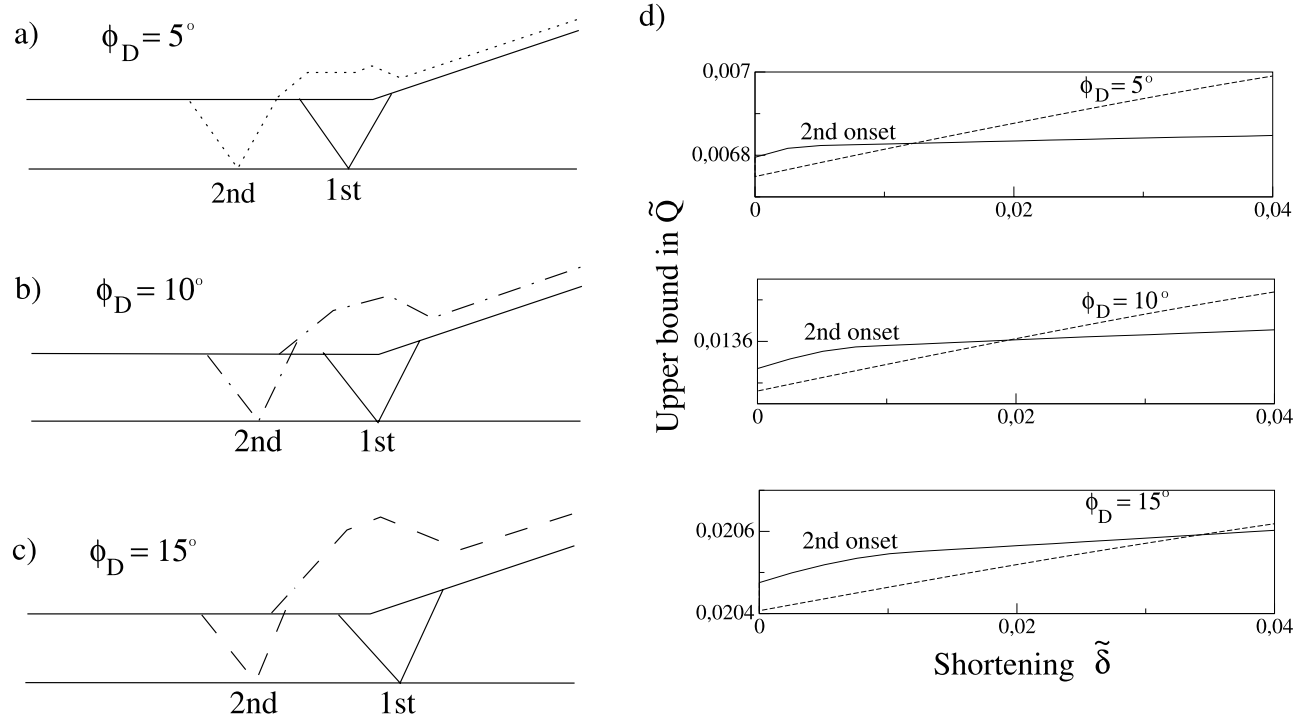


**Figure 11.** (a–c) The influence of $\phi_D$ on the lifetime of the first thrust and the position of the second thrust. (d) The predictions are based on the comparison of the various bounds in tectonic forces as a function of the shortening. The free surface slope $\alpha$ is 7.5° and the final friction angles over the ramp $\phi_{Rf}$ = 15° (0.27).

$\tilde{Q}$ are calculated, the first corresponding to the currently active ramp and the second corresponding to the initiation of a new ramp. When the latter is lower than the former, a new ramp is formed. Thus, the shortening at onset of the second ramp, i.e., the lifetime of the first ramp, is defined by the intersections with the solid curves. The main finding is that the lifetime of the first ramp, and therefore the amplitude of the relief due to the thrust fold, increases with the amount of weakening. This relation indirectly controls an important geological observable, the distance between the first and second ramps. This distance is seen to increase with ramp weakening in Figure 10, especially for the normal sequence.

[40] The last parameter studied here is the décollement friction angle. Results are presented in Figure 11 for an initial slope $\alpha$ set to 7.5°, $\phi_{Rf}$ set to 15° (0.27), and $\phi_D$ set to either 5° (0.09), 10° (0.18), or 15° (0.27). The least upper bound in tectonic force for the three values of $\phi_D$ are presented as function of $\tilde{\delta}$ in Figure 11d for the first thrust during its lifetime (dashed curve) and for the onset of the second thrust (solid curve). The three intersections reported demonstrate that the lifetime of the first thrust increases with increasing basal friction. The reason is that the onset of a second thrust ahead of the first one increases the length of the basal décollement and thus the work associated with its activation. Increasing the friction angle $\phi_D$ increases this difference in work and requires more relief buildup before the second thrust system becomes preferential. The more relief is necessary, the more shortening is required, implying a longer lifetime of the thrust. Note also that $\phi_D$ has an effect on the position of the first ramp and the distance to the second thrust. The first ramp is more to the rear and the distance larger for larger $\phi_D$. The first effect is certainly due to the necessity to shorten the activated décollement and the second controlled by the slope discontinuity due to the larger relief buildup, for larger $\phi_D$. A similar influence of $\alpha$ on the position of the first thrust is also observed in Figure 9.

### 4.2. Sequence of Thrusts

[41] The development of several thrusts in a normal sequence is now discussed. In all examples, the shortening occurs until the first out of sequence event is detected. The two slopes are set to $\alpha = 4.5°$, $\beta = 3°$, and the friction angles to $\phi_D = 5°$ (0.09), $\phi_{Ri} = 30°$ (0.58), $\phi_{Rf} = 15°$(0.27) so that the critical taper is $\alpha_c = 3.5°$ for the weakened ramp. The wedge is thus always subcritical. Note that weakening over the ramp is instantaneous ($\delta_T = 0$).

[42] Figure 12a illustrates the complete evolution of the sequence of thrusting in four stages. The two lines parallel to the surface are passive markers. The thin solid segments are the active thrust and back thrust and the dashed segments represent the deactivated ramps. Figure 12b presents the associated evolution of the tectonic upper bound in $\tilde{Q}$ as a function of the shortening $\tilde{\delta}$. The first graph in Figure 12a presents the initial state and the first thrust at its onset. Note that it is rooted on the basal décollement ahead of the topographic slope break because of the small basal friction. The evolution of the first thrust, T1, takes place until the shortening $\tilde{\delta}_1$ is reached. The jump recorded on the $\tilde{Q}$ ($\tilde{\delta}$) graph marks the activation of a second ramp, at the same load level as for the first thrust, and the instantaneous

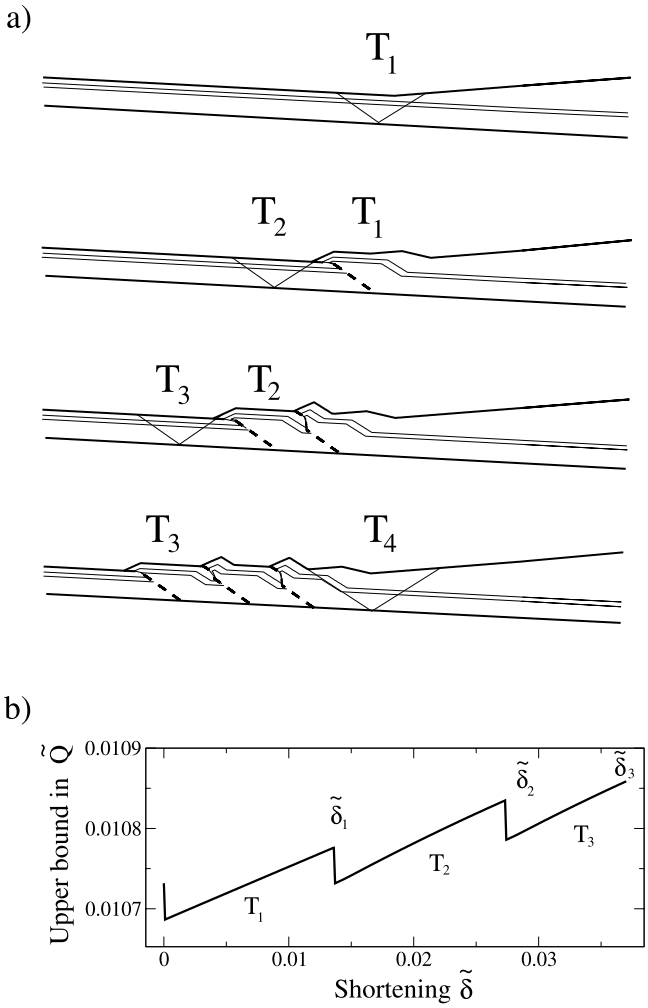


**Figure 12.** (a) Sequence of thrusting $T_1$ to $T_3$ ending with the first out of sequence thrust $T_4$ and (b) the evolution of the least upper bound on the tectonic force as a function of the amount of shortening $\tilde{\delta}$. The free surface slope $\alpha$ is 4.5°, the décollement dip is 3°, the friction angles are $\phi_{Rf}$ = 15° (0.27) and $\phi_D$ = 5° (0.09). The vertical and horizontal distances are at the same scale.

weakening since the transition length $\delta_T$ is set to zero. The position of this second thrust T2 at its onset is reported in the second graph in Figure 12a. The third graph corresponds to the arrest of the second thrust T2 and the onset of a third thrust ahead when the shortening is $\tilde{\delta}_2$. The third thrust T3, as the second, is rooted on the décollement such that the back thrust outcrops on the upper flat where the forelimb ends, approximately. The relief produced during the first and second thrusting events are equivalent so that the distance between the roots of T3 and T2 at the onset of T3 is approximately equal to the distance between the roots of T2 and T1 at the onset of T2. Note again the drop in the upper bound on the tectonic force at $\tilde{\delta}_2$, Figure 12b, because of the instantaneous weakening. Note also the complex topography above the oldest thrust T1, in the third graph of Figure 12a, because points there have been displaced either through one (T1) or two (T1 and T2) back thrusts. Thrust T3 ends for the shortening $\tilde{\delta}_3$ corresponding to the fourth graph in Figure 12a. For the first time, the new thrust T4 is out of sequence. This new system is between the oldest thrust T1 and the unperturbed wedge, i.e., in the region of greatest topographic depression. Note that the ramp outcrops exactly at the breaking point of the topography where the back thrust of T2 was last activated. Note also for the set of three thrusts in that sequence, that the passive markers show substantial thickening of the rocks which have been moved through the back thrusts to the hanging walls. This is the consequence of our optimization which does not find the back thrust to bisect the complementary angle of the ramp. Such assumption is classical with usual kinematic models that assume conservation of bed thickness but is not found here to be optimum. This thickening has been verified experimentally with sand [*Maillot and Koyi*, 2006] and further discussed for its geological relevance [*Koyi and Maillot*, 2007].

[43] The next item to be discussed for this sequence of thrusts is the dips of the ramp and back thrust, angles $\gamma$ and $\theta$ for the four events (Table 2). The general trend is that these two dips increase by 4° and decrease by 2.4°, respectively, for the first three events. The dips for the fourth event are more like those of the first thrust. The increase in ramp dip signals that more of the décollement is activated for thrusting in subsequent events. More décollement is required since the relief increases and the wedge in that region is like a perfect wedge with a slope $\alpha$ larger than the initial value. For the out of sequence event, the dips have to be close to those of the first event since they correspond to the same wedge in the back with an effective toe thickness which is slightly different. Note also that the mass in the hanging wall of T4 is larger then for T1. These differences explain the slight change in the dips values for the first and final thrusts.

[44] We finally examine the effect of ramp friction weakening and basal friction on the number of thrusts and the total shortening or total lifetime of the sequence before the first out of sequence event. Figure 13 shows the final topographic profiles of five examples including the reference one (fourth graph in Figure 12a is also Figure 13e) discussed above. As a general remark on these five different sequences, it should be noted that the back thrust (not drawn in this figure) of thrust $T_{n+1}$ in a normal sequence always outcrops on the upper flat near the front of the forelimb of thrust $T_n$. Two main quantitative differences are seen in that Figure 13. First, for low ramp friction weakening (Figure 13a), out of sequence thrusting occurs after a small shortening increment. This shortening increases as the difference $\phi_{Ri} - \phi_{Rf}$ increases from 5° (0.09) to 10° (0.18) and 15°(0.27) from Figure 13a to Figure 13c. This is of course consistent with the analysis of a single thrust: the more weakening on the

**Table 2.** Dips of the Ramp and Back Thrust for the Four Thrusting Events Constituting the Sequence Presented in Figure 12

| Thrust Event | Ramp Dip $\gamma$ | Back Thrust Dip $\theta$ |
|---|---|---|
| 1 | 32.3° | 32.0° |
| 2 | 33.6° | 32.8° |
| 3 | 36.3° | 34.4° |
| 4 | 32.9° | 31.9° |

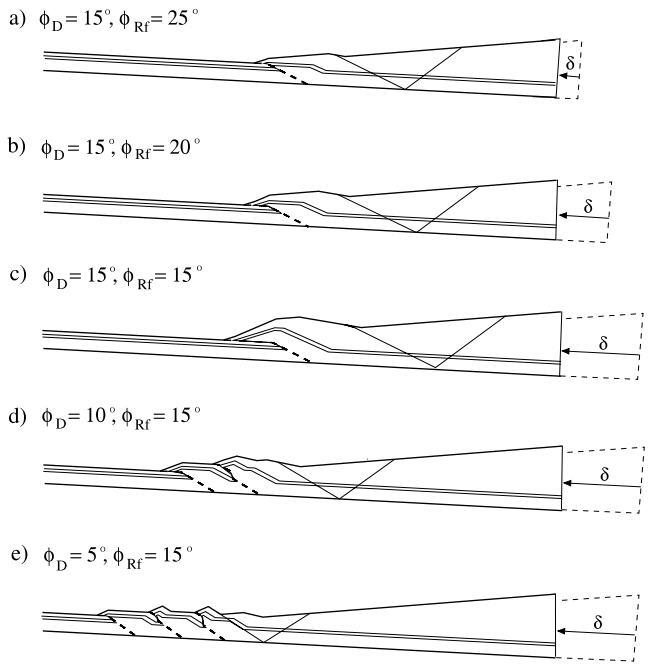


**Figure 13.** (a to c) The sequence of thrusting ending with the onset of the first out of sequence event, for different values of the friction angles $\phi_{Rf}$ and (d and e) two values of $\phi_D$. The surface slope $\alpha$ is 4.5° and the décollement dips at $\beta$ = 3°. The vertical and the horizontal distances are at the same scale.

ramp, the more relief is accumulated before a new thrust is preferred. Second, small basal friction (Figures 13d and 13e) promotes the development of numerous and closely spaced thrust ramps with a resulting relief buildup which is moderate but rather irregular. In contrast, large basal friction will produce a large and regular relief buildup (Figure 13c). Note that larger values of $\phi_D$ (e.g., 20°) leads to failure at the back wall (sub-critical wedge) which is not investigated in this contribution.

## 5. Application to the Nankai Accretionary Wedge

[45] The objective of this section is to test how the methodology proposed above can contribute to the interpretation of a concrete example and to infer with an inverse method if two thrust systems could be concurrently activated. The toe of the accretionary prism of Nankai, southeast coast of Japan, and more precisely the section revealed by the seismic reflection line NT62-8, presented by *Moore et al.* [1991], is considered. Three reasons motivate this choice. First, there is a convincing structural interpretation in the above reference as well as in the work of *Morgan and Karig* [1995]. Second, the toe of the prism is presently undergoing a transition between an active thrust and an incipient new structure in a normal sequence. This natural example illustrates the sequence of thrusting studied in the previous section in which the concurrent activity was marked by the intersection of the $\tilde{Q}$ versus $\tilde{\delta}$ curves in Figure 11d. The third reason is that there has been already a first attempt by *Schott and Koyi* [2001] to study that structure in terms of stress distribution and mechanical forces.

[46] The décollement, assumed straight ($\beta$ = 1.3°), the topography and the last two thrusts marked by their ramps, thin and thick solid lines for the formerly and the currently active ramp, respectively, are presented in Figure 14, which is modified from *Moore et al.* [1991]. The two parallel curvy solid lines, which bound the region of facies transition (between the trench fill and the Shikoku basin sediments), provide with their offset over the ramps an estimate of the accumulated shortening by thrusting. The ramps have more of an *s* shape than the straight segments proposed above. Moreover, *Morgan and Karig* [1995] advocate that the major part of the overall shortening is accommodated by diffuse deformation even in the foot wall of the active thrust. Such deformation was disregarded in our analysis. The incipient thrust, as proposed by *Morgan and Karig* [1995] and presented as a dotted line in Figure 14, has been positioned were the seismic reflectors are discontinuous in slope in the absence of a clear offset.

[47] *Koyi and Schott* [2001] proposed to compare the tectonic forces necessary for the active thrust and for the new, incipient thrust. These forces must be equal at the time of transfer of activity from the currently active to the incipient system. The analytical expression for these forces is due to *Mandal et al.* [1997] who proposed a simple polynomial stress distribution over the thrust. However, their stress field cannot satisfy point wise the Coulomb criterion over the ramp and thus is not statically admissible (equilibrium includes boundary conditions, the fault in that instance). To mitigate this deficiency, they suggested that the average tangential and normal forces do satisfy Coulomb criterion, leading to an expression for the compressive tectonic force. *Schott and Koyi* [2001], equating the tectonic forces for the active and incipient thrust, and knowing the geometry of the two thrusting systems, deduced then the friction coefficients along the décollement to be in the range of 5.7 to 9.1°.

[48] The above approach has definite merits despite our criticisms of the theoretical basis. Their selection of the active system is based on the comparison of the tectonic forces, a statement which is also made in our analysis. The major difference comes from the fact that neither the incipient thrust nor the currently active thrust proposed so far are optimum in the sense defined in this contribution. For example, the roots of their proposed ramps were not selected to provide the lowest upper bound in tectonic forces. This point is illustrated for the incipient thrust in Figure 14. There, our incipient thrust and back thrust (optimum with respect to the dips and the position of the root) have been drawn as dotted-dashed lines. This solution is made as close as possible to the observations of *Morgan and Karig* [1995], choosing by trial and error the friction angle $\phi_{Ri} = \phi_B$ (27.5°, 0.52) over the ramp and the friction angle over the décollement $\phi_D$ (11°, 0.19). These two angles are surprisingly close to the friction angles of (26.5° ± 5°, 0.50 ± 0.11) and (11° ± 5°, 0.19 ± 0.09) found by *Lallemand et al.* [1994] for the same section using the methodology of *Davis and von Huene* [1987] constructed with the same assumptions as *Dahlen* [1984]. It is of note that for the range of friction angle over the décollement proposed by *Schott and Koyi* [2001], the wedge is found supercritical

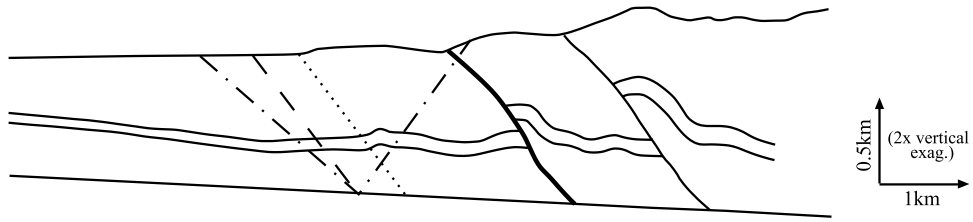


**Figure 14.** The toe of Nankai's prism according to the interpretation of *Moore et al.* [1991] of the seismic line NT62-8. The dotted line is the incipient ramp according to *Morgan and Karig* [1995]. The dashed line is the incipient ramp considered to build Figure 15 and is parallel to the dotted line and displaced toward the deformation front. It is where the ramp and back thrust, shown as dotted-dashed lines and obtained by optimization ($\phi_D$ = 11° (0.19), $\phi_{Ri} = \phi_B$ = 27.5° (0.52)), take also their root.

and the new incipient thrust should appear further to the front.

[49] This discrepancy between our optimum and the observed incipient thrust is not too surprising in view of the simplicity of our prototype compared to the heterogeneous mode of deformation outlined above. It is nevertheless proposed to continue our analysis, selecting the position and the orientation of the active and the incipient ramps according to the interpretation of the seismic profile presented by *Morgan and Karig* [1995], rather than according to the optimization, except for the dip of the back thrust which is difficult to observe on the seismic section. The final objective is still to decide whether or not the incipient and the currently active thrust are indeed concomitant. This decision requires to infer the range of potential friction angle values over the active ramp ($\phi_{Rf}$) and the incipient ramp ($\phi_{Ri}$). These computations are done assuming that these two angles can vary, independently, between zero and 90°, for a given value of the friction on the décollement. For each set of friction angles, the upper bounds for the active ramp (with friction $\phi_{Rf}$) and the incipient ramp ($\phi_{Ri}$) are computed. A given couple ($\phi_{Ri}$, $\phi_{Rf}$) is likely if the two respective bounds differ by less than some given percentage. The results of the calculation are the isocontours of relative difference (in percent) presented in Figure 15.

[50] Consider first the isocontours for $\phi_D$ = 1° obtained for one percent relative difference in tectonic force upper bounds. For an incipient ramp friction $\phi_{Ri}$ of say 40° (0.84), the friction angle over the active ramp $\phi_{Rf}$ has to be between 33 and 35° (0.65–0.70) so that the relative difference in force is less then one percent. There is thus a weakening along the active ramp in that instance, as suggested repeatedly in our forward theory. This conclusion is reversed if the décollement friction is set to $\phi_D$ = 5° (0.09). The angle $\phi_{Rf}$ is then contained in the interval [52°(1.28); 55°(1.43)]. There is thus hardening which is also observed for the isocontours of 5 percent for any point above the dotted line $\phi_{Ri} = \phi_{Rf}$ bisecting the plot. The trend for hardening with increasing décollement friction is confirmed with $\phi_D$ = 10° (0.18). It should be stressed again that such hardening is not possible with the theoretical evolution presented in the previous section. It is thus legitimate to question the hypotheses put forward to study this section through Nankai wedge. In particular, the hypothesis which is now challenged is the position of the incipient ramp.

[51] Figure 16 presents the results for an incipient ramp displaced by approximately 500 m toward the deformation front, dashed line in Figure 14, parallel to the one considered above (dotted lines in Figure 14). For example, for a friction angle of 10° (0.18) over the décollement, the friction over the active ramp is now between 32 (0.62) and 34° for $\phi_{Ri}$ set to 40°. These numbers appear to be more realistic then the range of 70 to 74° found in Figure 15. One observes also that the admissible values of $\phi_{Rf}$ are on a plateau of 7, 17, and 27° (0.67) for $\phi_D$ set to 1 (0.02), 5 (0.09), and 10° (0.18), respectively. This plateau indicates the strong influence of $\phi_D$ and the minor influence of $\phi_{Ri}$ on the selection of $\phi_{Rf}$. This minor influence of $\phi_{Ri}$, not observed on Figure 15, could be motivated by analogy with experimental results in the laboratory. The initial or peak friction angle $\phi_{Ri}$ is rather sensitive to the details of the

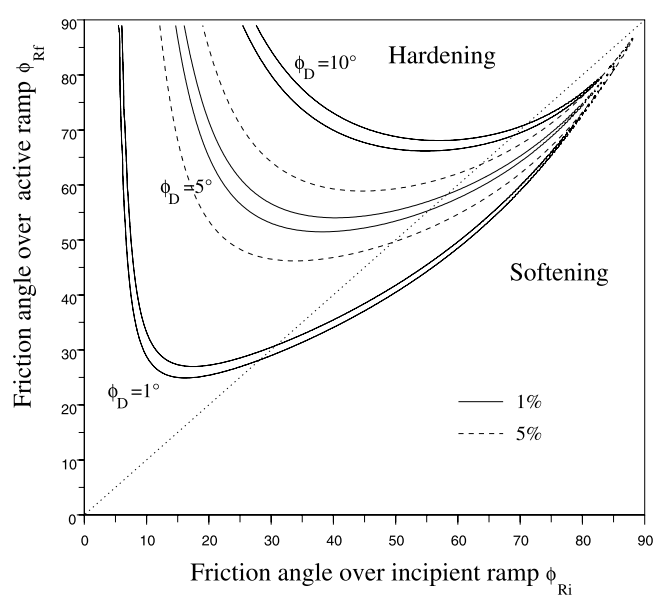


**Figure 15.** Isocontours of the relative difference, in percent, between the upper bounds in forces associated to the active ramp (thick solid line in Figure 14) and the incipient ramp suggested by *Morgan and Karig* [1995] (dotted line in Figure 14). The three one percent contours are for three values of the décollement friction angle. The five percent isocontour is plotted for $\phi_D$ = 5° only.

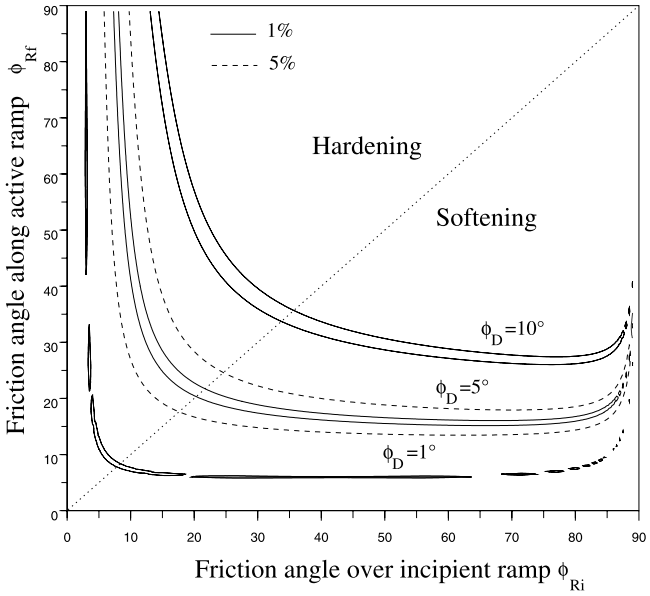


**Figure 16.** Isocontours of the relative difference, in percent, between the upper bound in tectonic forces associated to the active ramp (thick solid line in Figure 14) and the incipient ramp at the deformation front (dashed line in Figure 14). The three one percent contours are for three values of the décollement friction angle. The five percent isocontour is plotted for $\phi_D = 5°$.

loading device but should not influence the long-term structural response. Note also that the plateaux of Figure 16 are positioned in the softening domain. This observation is not a proof but is definitely consistent with our hypothesis for thrust event to have a finite life span.

[52] Another hypothesis which could have been challenged to improve our predictions is the constant value of the décollement friction $\phi_D$. A variation of the friction angle $\phi_D$ would have very likely contributed also to reconcile the observed and the optimum ramp position and dip. Fluid pressure change along the décollement could provide the physical basis for this heterogeneity [*Le Pichon et al.*, 1993].

[53] In conclusion, the complexity of the deformation processes, the fluid pressure distribution and the resulting strong heterogeneity at the toe of the prism require certainly a more sophisticated prototype for our inverse method in terms of geometry (shape of the discontinuities), spatial distribution of material properties (including cohesions), and mode of deformation (diffuse instead of localized). Despite these limitations which forbid us from applying a complete optimization, including especially the position of the incipient ramps, we have proposed an inverse method to assess the likeliness of a simultaneous activation of the active and incipient thrusts. This likeliness is based on the determination of possible values for the two friction angles over the active ($\phi_{Rf}$) and incipient ramps ($\phi_{Ri}$). It has been shown that $\phi_{Ri}$ is most likely larger then $\phi_{Rf}$ giving more merits to the assumption that weakening occurs over the ramp during the early stage of its life span. Although this softening has been largely documented in the laboratory, its application at the field scale does deserve some attentions. In that respect, it is surprising to see that a moderate change in the position of the incipient ramp has an important influence on the range of acceptable material parameters. The inverse method is thus very sensitive to the error on the observables. Consequently, a statistical description of the observables should be provided in the future to draw probabilistic conclusions on the two friction angles.

## 6. Merits and Limits of the Methodology

[54] The proposed strategy could be seen as a member of the large family of methods relying on dissipation or force criteria, as defined in section 1. In that respect, our method has several advantages and three are discussed. First, minimization of dissipation, which is not a law of physics, is replaced by the maximum strength theorem, which provides a theoretically rigorous upper bound on the total tectonic force. Second, ramps and back thrust are now no longer predefined, as in geometrical models, but are activated at the most favorable position and with the most favorable dip at any step of the evolution, as a consequence of the optimization of the upper bound. Third, the solution to the optimization requires only 1-D discretization of the surface and of the décollement. Memory requirements, number of floating point operations per time step, and implementation have no common measure with those required by the finite element or discrete element methods. A simulation, as those necessary to construct Figure 13e, takes a few tens of seconds on an average portable computer, and about 40 Kb of memory (surface topography and décollement being discretized by 2000 points each). The code is 1500 lines of Fortran 77, without recourse to any specific library. This numerical lightness makes it possible to explore the parametric space in a systematic manner as we did in the example of Nankai (approximately 25,000 optimizations of ramp-back thrust systems) or to use the method as a forward model in an inverse analysis.

[55] There are various limitations to the algorithms constructed here and three are now discussed. First, the dissipation is estimated only along discrete boundaries or faults disregarding bulk deformation which is often inferred, as in the case of Nankai's accretionary wedge. There, the thickness of the thrusts is decreasing with age revealing horizontal shortening once the thrust is abandoned. Extending the maximum strength theorem to account for bulk deformation limited by Coulomb criteria is certainly feasible [*Salençon*, 1974], although adding a certain complexity to the parametric study. It is certainly a necessary condition to avoid the drastic transfer of activity from one thrust to the next and thus to study two thrusts of concomitant activity. The second limitation is the extension of the proposed method to ductile materials which remains an open question. The third limitation is the disregard of fluid effects, crucial in accretionary wedges [*Le Pichon et al.*, 1993]. One could envision solving the fluid diffusion problem over the evolving structure and to modify locally the strength domain in terms of Terzaghi effective stress. This is an interesting research direction in view of the recent quantitative assessment of the influence of seepage forces on faulting directions monitored in sandbox experiments [*Mourgues and Cobbold*, 2003].

[56] The theory presented relies on the least upper bound in tectonic forces and it is proposed to use this specific solution as a physically plausible solution. The error is likely to be small if the kinematics is sufficiently rich to be close enough to reality. This error could be quantitatively estimated with a lower bound approach based on statically admissible (SA) stress field. The methodology is a direct application of the lower bound approach of limit analysis [*Salençon*, 1974]. The main difficulty is to span with sufficient accuracy the space of SA stress fields. The easiest way to proceed is by numerical means and, in 2-D, it consists of discretizing the domain of interest with triangular elements over which the stress is then linearly interpolated. The resulting equilibrium element method (EEM) then leads to a discrete optimization formulation of the problem which solution is a safe estimate (lower bound) to the applied load, appropriate for design in civil engineering [*Krabbenhøft et al.*, 2007]. The same EEM could be applied to many structural geology problems providing an error estimate as well as the stress distribution in folded structures (P. Souloumiac et al., Predicting stress in fault-bend fold by optimization, submitted to *Journal of Geophysical Research*, 2008).

## 7. Conclusion

[57] The objective of this paper was to demonstrate that the application of the maximum strength theorem provides estimates for the position of the active thrust, the dips of its ramp and back thrust, and the amount of shortening accommodated in its life span.

[58] The proposed methodology for the onset of thrusting was first validated by comparing favorably the predictions with the analytical results for the perfect triangular wedge studied by *Dahlen* [1984] and *Lehner* [1986]. A small perturbation is added to this perfect wedge in the form of a triangular relief. It is shown that there is a range of angles $\alpha$ for which the perturbation determines the position of the first thrust. This locking range is larger if the perturbation is toward the toe. If the perturbation is locking, its ends mark exactly where either the ramp or the back thrust are outcropping.

[59] Finite evolution was first studied with two simple thrusts having flat topography and décollement. The first thrust was with fast erosion so that no relief builds up and the geometry remains the one at the onset, except for the shortening of the back stop. It is found that weakening on the ramp influences the orientation of the back thrust up to $5-10°$. This is balanced in the presence of relief buildup because the additional weight acting on the ramp leads to the decrease of the back thrust dip. The overall dip variation is of a few degrees only and has minor influence on the tectonic force. This observation supports the idea that the dip of the back thrust could be kept constant during the study of more complex sequences of thrusts. Such sequence at the toe of the wedge is first studied for a single thrust which life span is defined by the amount of shortening accommodated before the next thrust is found. The first observation is that the life time of the first thrust would be zero unless some weakening of the ramp is accounted for. Indeed, the relief buildup beyond the onset contributes to an increase of the tectonic force which then becomes larger then the one obtained with a thrust infinitesimally close to the active system but still at its onset. Weakening is produced here by the decrease of the friction angle over the ramp from an initial value $\phi_{Ri}$ to the final value $\phi_{Rf}$ after a slip distance $\delta_T$, set to zero in most of the reported predictions. The introduction of this softening on the friction angle ensures thus a finite life time for each thrusting event since the decrease in friction leads to a drop in tectonic force which dominates initially over the increase necessary to lift the extra weight of the relief. It is then logical to find that the life span of a single thrust increases if the difference $\phi_{Ri} - \phi_{Rf}$ increases. Another parameter which controls the life span of a thrust is the friction angle over the décollement. The larger $\phi_D$ the longer is this life span. The reason is that the onset of a new thrust ahead of the active system requires slip over a larger section of the décollement. Increasing $\phi_D$ increases the work associated to that extra length and delays the time at which the new system will become preferable.

[60] Sequences of thrusting are then considered ending with the first out of sequence event. It is worth noting that the out of sequence is detected despite the absence of erosion, sedimentation, fluid pressure, or material properties lateral variations. For all these predictions, it is found that during the normal sequence, the next thrust has its back thrust always outcropping close to the termination of the forelimb of the current thrust. Increasing the friction angle over the décollement results in a smaller number of thrust in the normal sequence. Ramp weakening promotes a larger distance between successive ramps and larger overall shortening prior to the out of sequence event.

[61] The proposed methodology is then applied to construct an inverse method to detect the concomitant activity of two thrusts at the field scale, marked by the same upper bound in tectonic force. The section NT62-8 through Nankai's wedge, interpreted by *Moore et al.* [1991] and *Morgan and Karig* [1995], is considered and the concomitant activity signals the transfer from their active thrust to their incipient thrust. The inverse method relies on the determination of the likely values of the friction angles, initial for the incipient thrust, and final for the active system. The two main findings are as follows. First, it is shown that the ramps are not optimum in the sense defined in this paper based on a simple prototype with homogeneous mechanical properties. A heterogeneous décollement could reconcile this discrepancy. Second, the results confirmed that the friction over an incipient ramp is most likely larger then over a fully active ramp. The resulting weakening, a fundamental assumption in our work to warrant the finite life span of any thrust with relief buildup, is thus partly validated.

[62] The comparison of our predictions with analogue experiments results for the onset and the evolution is now in order. Concerning the onset, we obtain the same predictions for the stability of the perfect triangular wedge as the exact solution validated with analogue modeling by *Davis et al.* [1983]. Two comparisons are interesting concerning the evolution. First, the fact that the new back thrusts during the normal sequence are outcropping close to the forelimb of the previous thrust is observed in sandbox experiments by *Mulugeta* [1988] and *Mulugeta and Koyi* [1992]. Second, the spacing of the thrusts is smaller with smaller

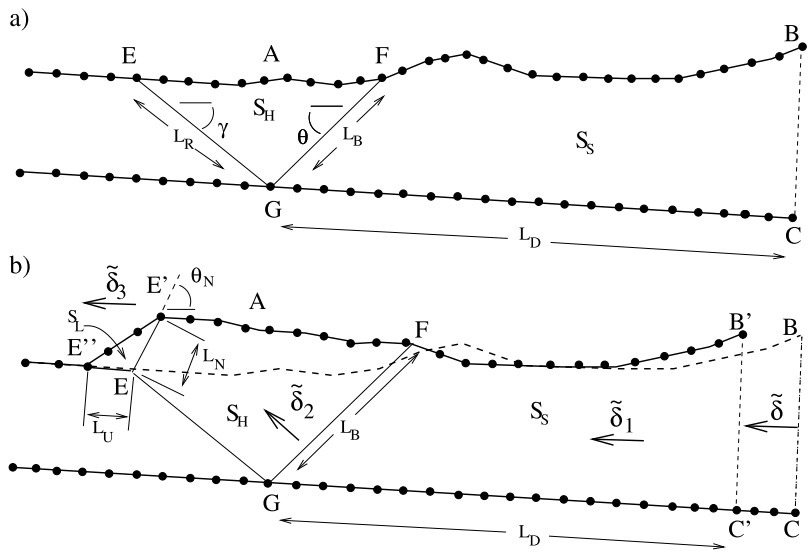


**Figure A1.** Illustration of the discretization of the topography and the décollement at the base of the numerical algorithm proposed to construct normal sequences of thrusting. (a) The mechanism of thrusting at the onset is composed of the ramp EG, the back thrust FG and part of the décollement GC. (b) The topographic points within the trust have been translated (with local exaggeration on top of the ramp) according to the zone they are leaving and entering, the back stop GC′B′F, the hanging wall EGFE′, and the forelimb EE′E″.

friction angles on the décollement. This is predicted by our theory and described in the experiments reported by *Gutscher et al.* [1998]. There is of course a great variation in the experimental results and the analogue benchmark proposed by *Schreurs et al.* [2006] is interesting to evaluate the strong variations in thrusting (position, number, lifetime of thrusts). In particular, the setup of the "push" and the "pull' type [*Dahlen and Barr*, 1989] are seen to provide different intensity in the localized deformation. This difference could be due to the friction on the lateral walls [e.g., *Costa and Vendeville*, 2004]. Preliminary experimental results (N. Cubas, Mechanics of folding in thrust-and-fold belts and in accretionary wedges, manuscript in preparation, 2008) show encouraging results in that direction and requires a full 3-D theoretical analysis (P. Souloumiac, Evolution of failure mechanisms in geological structures, manuscript in preparation, 2008), extending the present approach.

## Appendix A: Algorithm for the Construction of the Thrusting Sequences

[63] The algorithm to produce the sequence of thrusting relies on an incremental shortening from the rigid wall and is composed of three main tasks. As a preliminary, the initial topography and the basal décollement, which must be planar, are discretized into two series of points, solid dots in Figure A1a. The two surfaces are thus approximated by a series of straight segments. The first task is then to determine the position and dips of the first ramp and back thrust defined by the triplet of points (E, G, F). All triplets (E, G, F) consistent with dips in the range [0°, 90°] are considered by letting points E and F sweep through the discrete points of the topography, and point G, through the points of the décollement (Figure A1a). For each triplet, the value of $\tilde{Q}$ is calculated according to the general relation

$$\begin{aligned}\tilde{Q}\cos\phi_D \le{}& \tilde{S}_H\sin(\phi_R+\gamma)\tilde{U}_H + S_L\sin(\phi_U+\beta)\tilde{U}_L \\ &+ S_S\sin(\phi_D+\beta) + \tilde{c}_U\cos\phi_U\,\tilde{L}_U\tilde{U}_L + \tilde{c}_R\cos\phi_R\,\tilde{L}_R\tilde{U}_H \\ &+ \tilde{c}_D\cos\phi_D\,\tilde{L}_D + \tilde{c}_B\cos\phi_B\,\tilde{L}_B\tilde{J}_B + \tilde{c}_N\cos\phi_N\tilde{L}_N\tilde{J}_N,\end{aligned} \tag{A1}$$

with

$$\begin{aligned}\tilde{U}_H &= \frac{\sin(\beta+\phi_B+\theta+\phi_D)}{\sin(\gamma+\phi_B+\theta+\phi_R)}\,,\\ \tilde{J}_B &= \frac{\sin(\gamma+\phi_R-\beta-\phi_D)}{\sin(\gamma+\phi_B+\theta+\phi_R)}\,,\\ \tilde{J}_N &= \frac{\sin(\gamma+\phi_R-\beta+\phi_U)}{\sin(\theta_N+\phi_U+\beta-\phi_N)}\tilde{U}_H\,,\\ \tilde{U}_L &= \frac{\sin(\gamma+\phi_R+\theta_N-\phi_N)}{\sin(\beta+\phi_U+\theta_N-\phi_N)}\tilde{U}_H\,,\end{aligned}$$

taking $\phi_R = \phi_{Ri}$ for the ramp (segment EG), and setting $\tilde{L}_U = \tilde{L}_N = \tilde{L}_L = 0$. Surfaces $S_H$ and $S_S$ of the hanging wall and the back stop are bounded by polygonals and their area readily computed. The optimum triplet (E, G, F), defining the predicted active ramp and back thrust at the onset of shortening, is the one yielding the least $\tilde{Q}$. The second task is the evolution of the thrust, consequence of the shortening by the increment $\tilde{\delta}$ of the back stop. This evolution differs for points in three regions of the wedge. Topographic points which are part of the first region, the back stop (Figure A1b), are translated by $\tilde{\delta}_1 = \tilde{\delta}$ in the direction of the décollement. Topographic points in the second region, the hanging wall,

are translated parallel to the active ramp by the amount $\tilde{\delta}_2$ necessary to ensure mass flux conservation through the back thrust: the normal components to the back thrust of the first and second translations are equal. Topographic points in the third region, the forelimb, are translated in the direction of the upper flat (same as basal décollement). The amount $\tilde{\delta}_3$ of translation is again determined by requiring mass flux conservation through the normal fault separating the hanging walls of the ramp and the upper flat (line EE′ in Figure A1b). Points that change of region during translation follow relative amounts of each respective translation vector. For simplicity, the values of $\theta_N$ and $\theta$ are kept constant as shortening progresses despite the variation of the friction angle of the active ramp from $\phi_{Ri}$ to $\phi_{Rf}$, as discussed and justified in the main text. Note that point E, at the top of the active ramp, is immobile during evolution, but points E′, E″, and F are mobile. Areas of the three regions ($S_S$, $S_H$, $S_L$) and lengths of the five active bounding faults ($L_D$, $L_R$, $L_B$, $L_N$, $L_U$) are numerically calculated, and used to compute the current value of $\tilde{Q}$ with the general relation (A1) setting $\phi_R$ to $\phi_{Rf}$. Before proceeding to the next shortening increment, the third and last task considered is the possible onset of a new thrust. This possibility is checked in the same way as for the initial onset, by calculating the bounds in $\tilde{Q}$ associated to all possible triplets (E, G, F), sweeping through the current topography and with the friction angle $\phi_{Ri}$ on the potential new ramps (Figure A1a).

[64] It should be mentioned that this algorithm was designed with at least two simplifying assumptions, the first being that the upper flat is indeed flat and parallel to the décollement. The algorithm validity is then limited to ramps appearing frontward. The examples of evolution presented in the main text end as soon as a new active ramp is detected to the rear of the sequence. The second assumption is that the ramps are planar, precluding the reactivation of old ramps distorted if partly crossed through back thrusts. These limitations are inherent only to this algorithm and not to the general methodology proposed in this contribution and could thus be amended in the future.

[65] **Acknowledgments.** Helpful discussions with F.K. Lehner (University of Salzburg) and S. Lallemant (University of Cergy-Pontoise) throughout the development of this research are gratefully acknowledged.

## References

Buiter, S. J. H., A. Y. Babeyko, S. Ellis, T. V. Gerya, B. J. P. Kaus, A. Kellner, G. Schreurs, and Y. Yamada (2006), The numerical sandbox: Comparison of model results for a shortening and an extension experiment, in *Analogue and Numerical Modelling of Crustal-Scale Processes*, edited by S. J. H. Buiter and G. Schreurs, *Geol. Soc. London Spec. Publ.*, 253, 29–64.

Costa, E., and B. C. Vendeville (2004), Experimental insights on the geometry and kinematics of fold-and-thrust belts above weak, viscous evaporitic décollement: Reply to comments by H. Koyi and James Cotton, *J. Struct. Geol.*, *26*, 2139–2143, doi:10.1016/j-jsg.2004.04.002.

Dahlen, F. A. (1984), Noncohesive critical Coulomb wedges: An exact solution, *J. Geophys. Res.*, *89*(B12), 10,125–10,133.

Dahlen, F. A., and T. D. Barr (1989), Brittle frictional mountain building: 1. Deformation and mechanical energy budget, *J. Geophys. Res.*, *94*(B4), 3906–3922.

Davis, D., and R. von Huene (1987), Inferences on sediment strength and fault friction from structures at the Aleutian Trench, *Geology*, *15*, 517–522.

Davis, D., J. Suppe, and F. A. Dahlen (1983), Mechanics of fold-and-thrust belts and accretionary wedges, *J. Geophys. Res.*, *88*(B2), 1153–1172.

Del Castello, M., and M. L. Cooke (2007), Underthrusting-accretion cycle: Work budget as revealed by the boundary element method, *J. Geophys. Res.*, *112*, B12404, doi:10.1029/2007JB004997.

Erickson, S. G., and W. R. Jamison (1995), Viscous-plastic finite-element models of fault-bend folds, *J. Struct. Geol.*, *17*, 561–573.

Erickson, S. G., L. M. Strayer, and J. Suppe (2001), Initiation and reactivation of faults during movement over thrust-fault ramp: Numerical mechanical models, *J. Struct. Geol.*, *23*, 11–23.

Gutscher, M. A., N. Kukowski, J. Malavieille, and S. Lallemand (1998), Episodic imbricated thrusting and underthrusting: Analog experiments and mechanical analysis applied to the Alaskan Accretionary Wedge, *J. Geophys. Res.*, *103*(B5), 10,161–10,176.

Hafner, W. (1951), Stress distributions and faulting, *Bull. Geol. Soc. Am.*, *62*, 373–398.

Hardy, S., C. Duncan, J. Masek, and D. Brown (1998), Minimum work, fault activity and the growth of critical wedges in fold and thrust belts, *Basin Res.*, *10*, 365–373.

Koyi, H. A., and B. Maillot (2007), Tectonic thickening of hanging wall units over a ramp, *J. Struct. Geol.*, *29*, 924–932.

Koyi, H. A., and B. Schott (2001), Stress estimations from fault geometries applied to sand-box accretionary wedges, *Geophys. Res. Lett.*, *28*(6), 1087–1090.

Krabbenhøft, K., A. V. Lyamin, and S. W. Sloan (2007), Formulation and solution of some plasticity problems as conic programs, *Int. J. Solids Struct.*, *44*, 1533–1549.

Lallemand, S. E., P. Schnürle, and J. Malavieille (1994), Coulomb theory applied to accretionary and nonaccretionary wedges: Possible causes for tectonic erosion and/or frontal accretion, *J. Geophys. Res.*, *99*(B6), 12,033–12,055.

Lehner, F. K. (1986), Comments on "Noncohesive critical Coulomb wedges: An exact solution", *J. Geophys. Res.*, *91*(B1), 793–796.

Le Pichon, X., P. Henry, and S. Lallemant (1993), Accretion and erosion in subduction zones: The role of fluids, *Annu. Rev. Earth Planet. Sci.*, *21*, 307–331.

Lohrmann, J., N. Kukowski, J. Adam, and O. Oncken (2003), The impact of analogue material properties on the geometry, kinematics, and dynamics of convergent sand wedges, *J. Struct. Geol.*, *25*, 1691–1711.

Maillot, B., and H. Koyi (2006), Thrust dip and thrust refraction in fault-bend folds: Analogue models and theoretical predictions, *J. Struct. Geol.*, *28*, 36–49.

Maillot, B., and Y. M. Leroy (2003), Optimal dip based on dissipation of back thrusts and hinges in fold-and-thrust belts, *J. Geophys. Res.*, *108*(B6), 2320, doi:10.1029/2002JB002199.

Maillot, B., and Y. M. Leroy (2006), Kink-fold onset and development based on the maximum strength theorem, *J. Mech. Phys. Solids*, *54*, 2030–2059.

Maillot, B., C. Barnes, J.-M. Mengus, and J.-M. Daniel (2007), Constraints on friction coefficients by an inverse analysis of sand box thrust dips, *J. Struct. Geol.*, *29*, 117–128.

Mandal, N., A. Chattopadhyay, and S. Bose (1997), Imbricate thrust spacing: Experimental and theoretical analyses, in *Evolution of Geological Structures in Micro- to Macro-Scales*, edited by S. Sengupta, pp. 143–165, Chapman and Hall, London.

Masek, J. G., and C. C. Duncan (1998), Minimum-work mountain building, *J. Geophys. Res.*, *103*(B1), 907–917.

McTigue, D. F., and C. C. Mei (1981), Gravity-induced stresses near topography of small slope, *J. Geophys. Res.*, *86*(B10), 9268–9278.

Moore, G.F., D.E. Karig, T.H. Shipley, A. Taira, P.L. Stoffa, and W.T. Wood (1991), Strutural framework of the ODP leg 131 area, Nankaıuml; through 1991, *Proc. Ocean Drill. Program Init. Rep.*, *131*, 15–20.

Morgan, J. K., and D. E. Karig (1995), Kinematics and a balanced and restored cross-section across the toe of the eastern Nankai accretionary prism, *J. Struct. Geol.*, *17*, 31–45.

Morley, C. (1988), Out-of-sequence thrusts, *Tectonics*, *7*, 539–561.

Mourgues, R., and P. R. Cobbold (2003), Some tectonic consequences of fluid overpressures and seepage forces as demonstrated by sandbox modelling, *Tectonophysics*, *376*, 75–97.

Mulugeta, G. (1988), Modelling the geometry of Coulomb thrust wedges, *J. Struct. Geol.*, *10*, 847–859.

Mulugeta, G., and H. Koyi (1992), Episodic accretion and strain partitioning in a model sand wedge, *Tectonophysics*, *202*, 319–333.

Outtani, F. (1996), Cinématique, modélisation, et bilan énergétique des plis de rampe. Approche théorique et application à deux régions du Front Sud Atlasique, doctoral thesis, Univ. de Cergy-Pontoise, France.

Panian, J., and W. Pilant (1990), A possible explanation for foreland thrust propagation, *J. Geophys. Res.*, *95*(B6), 8607–8615.

Platt, J. (1988), The mechanics of frontal imbrication: A first order analysis, *Geol. Rdsch.*, *77*, 577–589.

Platt, J. (1990), Thrust mechanics in highly overpressured accretionary wedges, *J. Geophys. Res.*, *95*, 9025–9034.

Salençon, J. (1974), *Théorie de la Plasticité pour les Applications à la Mécanique des Sols*, Eyrolles, Paris. (English translation *Applications of the Theory of Plasticity in Soil Mechanics*, John Wiley, Chichester, U.K. 1977.)

Salençon, J. (2002), *De l'Élasto-Plasticité au Calcul à la Rupture*, Ellipses, Paris.

Schott, B., and H. Koyi (2001), Estimating basal friction in accretionary wedges from the geometry and spacing of frontal faults, *Earth Planet. Sci. Lett.*, *194*, 221–227.

Sciamanna, S., W. Sassi, R. Gambini, J. L. Rudkiewicz, F. Mosca, and C. Nicolai (2004), Predicting hydrocarbon generation and expulsion in the Southern Apennines Thrust Belt by 2D integrated structural and geochemical modeling: Part I-Structural and thermal evolution, in *Deformation, Fluid Flow, and Reservoir Appraisal in Foreland Fold and Thrust Belts*, *Heldberg Ser.*, vol. 1, edited by R. Swennen, F. Roure, and J. W. Granath, pp. 51–67, Am. Assoc. of Petrol. Geol., Tulsa, Okla.

Schreurs, G., et al. (2006), Analogue benchmarks of shortening and extension experiments, in *Analogue and Numerical Modelling of Crustal-Scale Processes*, edited by S. J. H. Buiter and G. Schreurs, *Geol. Soc. London Spec. Publ.*, 253, 1–27.

Suppe, J. (1983), Geometry and kinematics of fault-bend folding, *Am. J. Sci.*, *283*(7), 684–721.

Yin, A. (1993), Mechanics of wedge-shaped fault blocks: 1. An elastic solution for compressional wedges, *J. Geophys. Res.*, *98*(B8), 14,245–14,256.

Zoetemeijer, R., and W. Sassi (1992), 2D reconstruction of thrust evolution using the fault-bend fold method, in *Thrust Tectonics*, edited by K. R. McClay, pp. 133–140, Chapman and Hall, London.

N. Cubas and Y. M. Leroy, Laboratoire de Géologie, Ecole Normale Supérieure, UMR 8538, CNRS, 24 rue Lhomond, F-75231 Paris CEDEX 05, France. (cubas@geologie.ens.fr)

B. Maillot, Laboratoire de Tectonique, CNRS, Université de Cergy-Pontoise, F-95031 Cergy-Pontoise, France.